

Dark-ages reionization and galaxy formation simulation - III. Modelling galaxy formation and the epoch of reionization

Simon J. Mutch^{1*}, Paul M. Geil¹, Gregory B. Poole¹, Paul W. Angel¹,
Alan R. Duffy^{2,1}, Andrei Mesinger³, J. Stuart B. Wyithe¹

¹*School of Physics, The University of Melbourne, Parkville, VIC 3010, Australia*

²*Centre for Astrophysics and Supercomputing, Swinburne University of Technology, PO Box 218, Hawthorn, VIC 3122, Australia*

³*Scuola Normale Superiore, Piazza dei Cavalieri 7, I-56126 Pisa, Italy*

19 August 2016

ABSTRACT

We introduce MERAXES, a new, purpose-built semi-analytic galaxy formation model designed for studying galaxy growth during reionization. MERAXES is the first model of its type to include a temporally and spatially coupled treatment of reionization and is built upon a custom (100 Mpc)³ N -body simulation with high temporal and mass resolution, allowing us to resolve the galaxy and star formation physics relevant to early galaxy formation. Our fiducial model with supernova feedback reproduces the observed optical depth to electron scattering and evolution of the galaxy stellar mass function between $z=5$ and 7, predicting that a broad range of halo masses contribute to reionization. Using a constant escape fraction and global recombination rate, our model is unable to simultaneously match the observed ionizing emissivity at $z \lesssim 6$. However, the use of an evolving escape fraction of 0.05–0.1 at $z \sim 6$, increasing towards higher redshift, is able to satisfy these three constraints. We also demonstrate that photoionization suppression of low mass galaxy formation during reionization has only a small effect on the ionization history of the inter-galactic medium. This lack of ‘self-regulation’ arises due to the already efficient quenching of star formation by supernova feedback. It is only in models with gas supply-limited star formation that reionization feedback is effective at regulating galaxy growth. We similarly find that reionization has only a small effect on the stellar mass function, with no observationally detectable imprint at $M_* > 10^{7.5} M_\odot$. However, patchy reionization has significant effects on individual galaxy masses, with variations of factors of 2–3 at $z=5$ that correlate with environment.

Key words: galaxies: formation – galaxies: high redshift – dark ages, reionization, first stars

1 INTRODUCTION

There are several key observational areas in which substantial progress will be made in the study of the first galaxies during the coming decade. Of particular importance will be forthcoming programmes searching for galaxies beyond the current redshift frontier using the *Hubble Space Telescope* and, in the future, the *James Webb Space Telescope* (e.g. Bouwens et al. 2011; McLure et al. 2013; Schenker et al. 2013). However, even next generation surveys will not extend to the faint luminosities of the faintest galaxies thought to drive the reionization of inter-galactic neutral hydrogen

in the early Universe (Robertson et al. 2013; Duffy et al. 2014). Thus, alongside new probes provided by high redshift gamma-ray bursts (e.g. Trenti et al. 2015) and metal pollution of the inter-galactic medium (IGM; e.g. Díaz et al. 2014), an important new observational window for study of the first galaxies will be provided by experiments to measure the redshifted 21 cm radio signal (Furlanetto 2006; Morales & Wyithe 2010). These observations will both provide the first direct probe of the neutral hydrogen content in the high redshift Universe and, through modelling, provide a route to study the early dwarf galaxies thought to exist during reionization alongside their more massive counterparts whose star formation can be directly detected.

Within this context, the development of theoretical

* E-mail: smutch@unimelb.edu.au

models that include a self-consistent treatment of the physics of galaxy formation and intergalactic hydrogen will play a key role. Traditional approaches to the study of galaxies and their effects on the IGM utilize either numerical simulation or analytic modelling. The latter allows investigation of average behaviours on large scales but the calculations are inherently linear, meaning that complex feedback processes cannot be addressed (e.g. Furlanetto et al. 2004; Wyithe & Loeb 2004, 2013). Numerical simulations, on the other hand, include non-linear effects but at the expense of computational cost. To achieve a volume sufficiently large to study ionized structure, a popular and effective approach to simulating reionization is to begin with a collisionless N -body simulation (e.g. Ciardi et al. 2003; Sokasian et al. 2003; Iliev et al. 2007, 2008; Trac & Cen 2007; Zahn et al. 2007; Shin et al. 2008; Trac et al. 2008) and use a simple prescription to relate halo mass to ionizing luminosity. A radiative transfer method (for example ray-tracing algorithms) can then be used to calculate the ionization structure on large scales. In recent years, new hybrid, or semi-numerical models (Mesinger & Furlanetto 2007; Geil & Wyithe 2008; Kim et al. 2013a) have been developed that combine N -body simulations with analytical methods to enable the calculation of reionization structure in very large volumes with high efficiency. These methods have elucidated the primary features of the ionization structure during reionization, but do not capture the physics of galaxy formation.

Therefore, to better understand the physics of galaxy formation, many authors have performed hydrodynamic simulations of galaxy formation (Finlator et al. 2011; Salvaterra et al. 2011; Jaacks et al. 2012, e.g.) which are able to directly model the growth of stellar mass in high-redshift galaxies when coupled with sub-grid models for processes including metal enrichment and feedback. These simulations are able to broadly reproduce the luminosity function of galaxies at high redshift, however, computational expense limits their ability to self-consistently model reionization in volumes large enough to statistically describe the spatial evolution of this process. Instead, a common approach is to impose a simple parametrized model to approximate the average ionizing background as a function of redshift, independent of the properties of the ionizing source population (e.g. Feng et al. 2016) or their spatial distribution (e.g. Genel et al. 2014; Schaye et al. 2015). Recently, hydrodynamical simulations of galaxy formation with coupled radiative transfer have been used to compute the effects of reionization on galaxy formation self-consistently for the first time (e.g. So et al. 2014; Norman et al. 2015; Ocvirk et al. 2015; Pawlik et al. 2015). However, the extreme computational expense of these simulations limit their size to relatively small volumes and/or few variations on galaxy formation physics or reionization scenarios that can be explored. In addition, the modelling of sub-grid physical processes remains uncertain, requiring systematic studies of the available parameter space in order to draw robust conclusions. Such studies represent an extreme computational challenge which has yet to be overcome.

Another approach to the realistic modelling of high redshift galaxies has been through the use of semi-analytic galaxy formation models (Benson et al. 2006; Lacey et al. 2011; Račević et al. 2011; Zhou et al. 2013). While large volumes are available to such models, until now they have

not been fully coupled to an accurate description of reionization. This is in part due to the structure of most existing semi-analytic models, which utilize so-called ‘vertical’ halo merger trees (e.g. Springel et al. 2005; Bower et al. 2006; Harker et al. 2006; De Lucia & Blaizot 2007) in which galaxies belonging to each tree branch are evolved independently from the rest of the simulation volume. Since galaxies drive the process of reionization, which in turn affects their subsequent evolution, galaxies spatially separated by tens of Mpc cannot be considered and evolved independently as has traditionally been the case (Wyithe & Loeb 2004). Self-consistently studying reionization instead requires a semi-analytic model designed to run on ‘horizontal’ merger trees where all haloes at each snapshot of the parent N -body simulation are processed simultaneously. Additionally, the reduced dynamical time of dark matter haloes at high redshift requires snapshots with a much higher cadence than is needed to model galaxy formation at lower redshifts.

This is the third paper in a series describing the Dark Ages Reionization And Galaxy Observables from Numerical Simulations (DRAGONS) project¹, which integrates detailed semi-analytic models constructed specifically to study galaxy formation at high redshift, with semi-numerical models of the galaxy–reionization process interaction. In this work, we introduce MERAXES, the new semi-analytic model of galaxy formation developed for DRAGONS, integrating the 21CMFAST semi-numerical model for ionization structure described in Mesinger & Furlanetto (2007). MERAXES is implemented within the large-volume, high-resolution, and high-cadence *Tiamat* N -body simulation described in Poole et al. (2016, hereafter Paper I) and Angel et al. (2016, Paper II). In subsequent papers we will use MERAXES to carry out a range of studies including the investigation of the high redshift galaxy luminosity function (Liu et al. 2015, Paper IV), and the ionization structure of the IGM (Geil et al. 2015, Paper V). Complimentary, high resolution hydrodynamic simulations are described in Duffy et al. (2014).

The outline of the paper is as follows. In Section 2 we provide a full description of MERAXES including an overview of the *Tiamat* simulation and associated merger trees which act as input for our semi-analytic model, the physical prescriptions employed, and the methodology of our reionization coupling and the integration of 21CMFAST. In Section 3 we then go on to describe the calibration of the model’s free parameters against the evolution of the high-redshift galaxy stellar mass function. In Section 4 we investigate a range of different extreme reionization and galaxy physics modifications in order to elucidate the roles of reionization suppression and galactic feedback processes in the build up of stellar mass and the evolution of the global neutral hydrogen fraction. We also highlight the important consequences of utilizing a patchy, self-consistent reionization model compared to more commonly employed, parametrized descriptions of reionization. Finally, in Section 5 we summarize our study and conclusions. Throughout this work, we employ a standard, spatially flat Λ cold dark matter cosmology with the most up-to-date cosmological parameters as determined by Planck Collaboration (2015): $(h, \Omega_m, \Omega_b, \Omega_\Lambda, \sigma_8, n_s) = (0.678, 0.308, 0.0484, 0.692, 0.815, 0.968)$.

¹ <http://dragons.ph.unimelb.edu.au/>

2 MERAXES

Modern semi-analytic galaxy formation models are capable of providing statistically accurate representations of the global properties of galaxies across a broad range of redshifts (e.g. [Baugh 2006](#); [Mutch et al. 2013](#); [Henriques et al. 2015](#)), and are therefore able to describe the distribution and evolution of the ionizing photons which drive the process of cosmic reionization. These photons generate regions of ionized hydrogen (H II) with characteristic sizes of tens of Mpc during reionization ([Wyithe & Loeb 2004](#)). Thus, in order to take advantage of this information and to self-consistently model the effect of these photons on the growth of galaxies, one must consider the contributions of galaxies separated by similar scales.

Traditionally, semi-analytic models have therefore used parametrized descriptions to include the average effect of reionization and the associated photo-suppression of baryonic infall on the growth of galaxies ([Benson et al. 2006](#); [Croton et al. 2006](#); [Somerville et al. 2008](#)). These parametrizations are typically calibrated using radiative transfer simulations and are provided as a function of redshift and halo mass alone (e.g. [Gnedin 2000](#)). Whilst it is computationally efficient to include reionization in this manner, there are a number of important drawbacks. First, the progression of reionization is not self-consistently modified by the growth of the galaxies which are driving it. Therefore it is impossible to investigate how different galaxy physics affect the ionization state of the IGM or to quantify the potential back-reaction on galaxy evolution. Secondly, these simple reionization prescriptions miss the potentially important effects of spatially dependent self-regulation ([Iliev et al. 2007](#); [Sobacchi & Mesinger 2013](#)), whereby massive galaxies located at the peaks in the density distribution can reionize their surroundings, delaying or preventing the onset of star formation in nearby lower mass haloes.

Our new semi-analytic galaxy formation model, MERAXES, has been written from the ground up to facilitate these modelling requirements. Its key features include the ‘horizontal’ processing of merger trees constructed from a purpose run N -body simulation (*Tiamat*; see Section 2.1 below) and the incorporation of the semi-numerical reionization algorithm, 21CMFAST, as a core component. When combined, these features allow MERAXES to efficiently couple the growth of galaxies to the process of reionization, both temporally and spatially. It can therefore be used to investigate the potentially complex effects of various reionization models on the properties of high- z galaxies, as well as to test for observational discriminants of different galaxy physics in the distribution and evolution of inter-galactic neutral hydrogen.

In order to develop confidence in our newly developed framework, as well as provide a solid foundation for future additions and improvements, our initial implementation of the baryonic physics processes in MERAXES is heavily based on the well-studied L-GALAXIES semi-analytic model ([Kauffmann 1996](#); [De Lucia & Blaizot 2007](#); [Guo et al. 2013](#); [Henriques et al. 2015](#)), in particular the version described in [Croton et al. \(2006\)](#) and extended in [Guo et al. \(2011\)](#). However, as well as our improved treatment of reionization, the excellent temporal resolution provided to us by the *Tiamat* merger trees has also necessitated the development of a

number of important updates to the treatment of supernova feedback and stellar mass recycling.

In the following sub-sections we describe MERAXES in full, including its input data set in the form of halo merger trees extracted from the *Tiamat* N -body simulation, the details of the implemented galaxy physics prescriptions, and our methodology for integrating 21CMFAST to self-consistently model reionization.

2.1 Input – the *Tiamat* N -body simulations

The *Tiamat* collisionless N -body simulation has been designed for the DRAGONS study of high-redshift galaxy formation and the epoch of reionization (EoR). It contains 2160^3 dark matter particles within a 100Mpc (comoving) periodic box and was run using a modified version of the GADGET-2 N -body code and the latest *Planck* 2015 ([Planck Collaboration 2015](#)) cosmology. The volume of *Tiamat* allows for the investigation of the statistical signatures of reionization and its 21cm observational signal, whilst the resulting particle mass of $3.89 \times 10^6 M_\odot$ provides the necessary resolution to identify the low-mass sources thought to be driving this process. Furthermore, *Tiamat* provides high temporal resolution in the form of 100 output snapshots evenly spaced in cosmic time between $z=35$ and 5, resulting in a cadence of 11.1Myr per snapshot. This level of temporal resolution is a unique feature of *Tiamat* which allows our semi-analytic model to accurately simulate the stochastic nature of star formation in a regime where the dynamical time of a typical galactic disc is shorter than the lifetime of the least massive Type II supernova progenitor (~ 40 Myr).

In addition to the main *Tiamat* volume, a suite of smaller, higher mass resolution N -body simulations have been run as part of the DRAGONS programme (Paper-I). For this work we make particular use of the *Tiny Tiamat* and *Medi Tiamat* volumes in order to quantify the effect of resolution on our results (see Section 4.1 and Appendix A). *Tiny Tiamat* is the highest resolution simulation of the DRAGONS suite, with a particle mass of $10^5 M_\odot$ in a small box of side length 14.8Mpc, whilst *Medi Tiamat* bridges the resolution gap with the main simulation by providing a particle mass of $1.16 \times 10^6 M_\odot$ in a 33.3Mpc box. Both simulations maintain the same snapshot cadence as the main *Tiamat* volume and are described in detail in Paper-I.

Halo identification in all simulations used in this work was carried out using the SUBFIND ([Springel et al. 2001](#)) real-space halo finder down to a minimum mass of 32 particles (corresponding to 3.71×10^8 , 1.25×10^8 , $3.2 \times 10^6 M_\odot$ for *Tiamat*, *Medi Tiamat*, and *Tiny Tiamat* respectively). The resulting halo catalogues comprise of friends-of-friends (FoF) groups of gravitationally bound particles which themselves are made up of a single mass dominant ‘central’ subhalo along with zero or more sub-dominant ‘satellite’ subhaloes. For further details, interested readers are referred to Papers I and II.

2.1.1 Merger trees

The formation history of subhaloes, in the form of hierarchical merger trees, acts as the raw input to MERAXES and

is used to define the positions and growth of galaxies. Many traditional semi-analytic models, such as the L-GALAXIES (e.g. De Lucia & Blaizot 2007; Guo et al. 2011; Henriques et al. 2015) and GALFORM (e.g. Bower et al. 2006; Lagos et al. 2012; Kim et al. 2013b) variants, process such trees in a depth-first (or ‘vertical’) order, whereby small collections of directly interacting dark matter haloes are processed one after the other from high to low redshift and independently of each other. Whilst computationally efficient in terms of minimizing the memory overhead required to process the simulation, the inherent assumption is that haloes (and by extension galaxies) which do not directly interact do not affect each other’s evolution. This assumption breaks down when considering the process of reionization during which ionizing photons from galaxies tens of Mpc away can heat the IGM, raising the local Jeans mass and altering the accretion rate of baryons (Dijkstra et al. 2004). MERAXES instead processes trees breadth-first (or ‘horizontally’). In this method all of the haloes in the entire volume are loaded into memory and the associated galaxies evolved for each snapshot sequentially. This allows MERAXES to more efficiently model reionization than previous comparable works (e.g. Kim et al. 2013a). More detailed information, including the precise details of our merger tree construction technique, can be found in Poole et al. (in preparation).

2.2 Baryonic infall

We begin by making the standard assumption that as FoF groups grow, any freshly accreted mass, always carries with it the universal baryon fraction, $f_b = \Omega_b / \Omega_m$, in the form of pristine primordial gas. However, the fraction of these infalling baryons which will remain bound to the FoF group and participate in galaxy formation may be reduced by a number of factors. In particular, ionizing ultraviolet background (UVB) radiation from both local and external sources can heat the IGM, increasing the local Jeans mass and leading to a non-negligible reduction in the amount of baryons successfully captured by low mass systems (Dijkstra et al. 2004). We parametrize this reduction in terms of a baryon fraction modifier, f_{mod} , which represents the attenuation of the total baryon mass that could have ever been successfully captured by an FoF group in its lifetime:

$$m_{\text{infall}} = f_{\text{mod}} f_b M_{\text{vir}} - \sum_{i=0}^{N_{\text{gal}}-1} m_*^i + m_{\text{cold}}^i + m_{\text{hot}}^i + m_{\text{ejected}}^i, \quad (1)$$

where m_{infall} is the infalling baryonic mass, $0 \leq f_{\text{mod}} \leq 1$, and N_{gal} is the number of galaxies in the FoF group. The baryonic reservoirs m_* , m_{cold}^i , m_{hot}^i , and m_{ejected}^i are described in the following sections along with the physical prescriptions which govern their evolution. If the mass of the FoF group or the value of f_{mod} decreases then it is possible for m_{infall} to become negative. In this case baryons are stripped from the system as described in Section 2.8. An accurate spatially and temporally dependent calculation of the value of f_{mod} is a key feature of MERAXES and a subject which we return to in detail in Section 2.11.

Any baryons which are successfully captured are assumed to be shocked to the virial temperature of the host FoF group and added to a diffuse hydrostatic hot reservoir where they mix with any already present hot gas.

2.3 Cooling

At each time step in the simulation some fraction of the hydrostatic hot reservoir may cool and condense down into the central regions of the group where it can then participate in galaxy formation. In order to calculate the rate at which this occurs we follow the commonly employed methodology outlined in White & Frenk (1991). In this model, the cooling time of a quasi-static isothermal hot halo is given by the ratio of the specific thermal energy to cooling rate per unit volume:

$$t_{\text{cool}}(r) = \frac{1.5 \bar{\mu} m_p k T}{\rho_{\text{hot}}(r) \Lambda(T, Z)}, \quad (2)$$

where $\bar{\mu} m_p$ is the mean particle mass (9.868×10^{-25} g for a fully ionized gas), k is the Boltzmann constant, Λ is the cooling function (Sutherland & Dopita 1993), T is the temperature of the gas and $\rho_{\text{hot}}(r)$ is its density profile. As mentioned above, we assume that the hot gas is shocked to the virial temperature of the FoF group, therefore we set $T = T_{\text{vir}} = 35.9 (V_{\text{vir}} / \text{kms}^{-1})^2 \text{K}$. For simplicity, we also assume that the hot gas follows a singular isothermal sphere density profile:

$$\rho_{\text{hot}}(r) = \frac{m_{\text{hot}}}{4\pi R_{\text{vir}} r^2}. \quad (3)$$

With knowledge of the cooling time, we can define an appropriate cooling radius, r_{cool} , within which there is enough time for the material to lose pressure support and condense to the system centre. Following Croton et al. (2006), we take this to be the radius at which t_{cool} is equal to the dynamical time of the host FoF group, $t_{\text{dyn}}^{\text{FoF}} = R_{\text{vir}} / V_{\text{vir}}$. As discussed by White & Frenk (1991), this model for cooling naturally leads to three distinct regimes.

(i) When $r_{\text{cool}} \geq R_{\text{vir}}$, any infalling gas will cool so rapidly that there will be no time for a stable shock to form and thus for the gas to reach hydrostatic equilibrium. In this case we assume that the infalling material flows directly into the central regions of the halo over a dynamical (free-fall) time, $\dot{m}_{\text{cool}} = \dot{m}_{\text{hot}} / t_{\text{dyn}}$.

(ii) When $r_{\text{cool}} < R_{\text{vir}}$ the cooling time will be sufficiently long that a quasi-static hot atmosphere will form. The cooling rate from this atmosphere can then be calculated from a simple continuity equation for the mass flux across the evolving cooling radius:

$$\begin{aligned} \dot{m}_{\text{cool}} &= 4\pi \rho_{\text{hot}}(r_{\text{cool}}) r_{\text{cool}}^2 \dot{r}_{\text{cool}} \\ &= m_{\text{hot}} \frac{r_{\text{cool}}}{R_{\text{vir}}} \frac{1}{t_{\text{dyn}}^{\text{FoF}}} \end{aligned} \quad (4)$$

(iii) When $T_{\text{vir}} \leq 10^4 \text{K}$, we set $r_{\text{cool}} = 0$ and no cooling occurs. In the standard model of galaxy formation, haloes with this temperature represent the lowest mass scale for galaxy formation. Below this, the primary mechanism for gas cooling is via molecular hydrogen which is easily photo-dissociated by trace amounts of star formation, making it an inefficient pathway for Pop II star formation. Above this temperature, atomic line cooling provides an efficient mechanism to dissipate energy and remove pressure support (Barkana & Loeb 2001). The mass resolution of our input N -body simulation, *Tiamat*, was chosen such that the minimum halo mass at $z=5$ is close to the atomic cooling mass threshold of $T_{\text{vir}} = 10^4 \text{K}$. Although earlier Pop III and Pop II

star formation is possible in smaller haloes, the level of contribution of these objects to reionization remains unclear, being heavily dependent on the masses of the first supernovae which could potentially delay future star formation by tens to hundreds of Myr (e.g. [Chen et al. 2014](#); [Jeon et al. 2014](#)). We therefore do not include these objects in our current model.

All material which successfully cools into the central regions of the FoF group is assumed to be deposited directly into the cold gas reservoir of the galaxy hosted by the central halo. This assumption is commonly employed by a number of other semi-analytic models (e.g. [Bower et al. 2006](#); [De Lucia & Blaizot 2007](#); [Somerville et al. 2008](#); [Lu et al. 2011a](#)) which utilize halo catalogues created by the SUBFIND halo finder. It is also warranted in the vast majority of systems where the central halo dominates the mass of the FoF group and ensures a physically meaningful match between the galaxy formation physics of MERAXES and the substructure hierarchy produced by the halo finder employed for this programme (see Paper I where this issue is raised).

2.4 Star formation

As discussed in the previous section, gas which cools from the FoF group hot reservoir is assumed to be deposited into the galaxy hosted by the central halo of the group. Here we assume that it settles into a rotationally supported cold gas disc with an exponential surface density profile. Under the simplifying assumption of full conservation of specific angular momentum, the scale radius of the disc can be approximated from the spin of the host dark matter halo, λ , to be $r_s = R_{\text{vir}}(\lambda/\sqrt{2})$, where we use the definition of λ provided by [Bullock et al. \(2001\)](#).

Based on the well-established observational work of [Kennicutt \(1998\)](#), the star formation rate of local spiral galaxies can be related to the surface density of cold gas above a given threshold. The value of this threshold can be understood in terms of the gravitational instability required to form massive star-forming clouds ([Kennicutt 1989](#)). Assuming a constant gas velocity dispersion and a flat rotation curve with a circular velocity equal to that of the host dark matter halo, V_{vir} , [Kauffmann \(1996\)](#) demonstrated that this stability criterion can be expressed as

$$\Sigma_{\text{crit}}(r) = \Sigma_{\text{norm}} \left(\frac{V_{\text{vir}}}{\text{km s}^{-1}} \right) \left(\frac{r}{\text{kpc}} \right)^{-1} M_{\odot} \text{pc}^{-2}. \quad (5)$$

[Kauffmann \(1996\)](#) originally assumed a thin isothermal disc with a gas velocity dispersion appropriate for low-redshift spiral galaxies of 6 km s^{-1} , resulting in $\Sigma_{\text{norm}} = 0.59$. However, both observations and simulations of high-redshift star forming galaxies indicate that they typically possess highly turbulent, clumpy discs (e.g. [Wisnioski et al. 2011](#); [Glazebrook 2013](#); [Bournaud et al. 2014](#)). This suggests the need for a modified Σ_{norm} value. Given the uncertainty in what value this should take, we choose to leave it as a free parameter in our model. We note that [Henriques et al. \(2015\)](#) also advocate allowing freedom in the choice of Σ_{norm} ; however, they instead motivate this by the observation that star formation is more closely linked to molecular, rather than total, gas density (e.g. [Leroy et al. 2008](#)). This suggests that

the surface density of total gas required for star formation could plausibly be lower than the [Kauffmann \(1996\)](#) value.

Equation (5) can be converted to a total critical mass, m_{crit} , by integrating out to the disc radius, r_{disc} :

$$m_{\text{crit}} = 2\pi \Sigma_{\text{norm}} \left(\frac{V_{\text{vir}}}{\text{km s}^{-1}} \right) \left(\frac{r_{\text{disc}}}{\text{kpc}} \right) 10^6 M_{\odot}. \quad (6)$$

Following [Croton et al. \(2006\)](#), we assume $r_{\text{disc}} = 3r_s$. The factor of 3 was chosen by [Croton et al. \(2006\)](#) based on the properties of the Milky Way and therefore may not be representative of the high-redshift galaxies which we consider in this work. However, instead of considering this to be another free parameter of the model we note that $m_{\text{crit}} \propto \Sigma_{\text{norm}} r_{\text{disc}}$, meaning any such freedom can already be considered to be included in Σ_{norm} . In future work, we will compare our predicted disc sizes to high- z observations and investigate the success of these simple scaling relations in detail.

If the total amount of cold gas in the disc is greater than the critical mass, the star formation rate is assumed to be given by

$$\dot{m}_* = \alpha_{\text{SF}} \frac{(m_{\text{cold}} - m_{\text{crit}})}{t_{\text{dyn}}^{\text{disc}}}, \quad (7)$$

where $t_{\text{dyn}}^{\text{disc}} = r_{\text{disc}}/V_{\text{vir}}$ is the dynamical time of the disc and α_{SF} is a free parameter describing the efficiency of star formation in the form of the formation time-scale in units of the dynamical time.

In summary, the star formation prescription we employ in MERAXES is almost identical to that of [Croton et al. \(2006\)](#) with the addition of Σ_{norm} as an extra free parameter (as previously advocated by [Henriques et al. 2015](#)).

2.5 Supernova feedback

The radiative and mechanical energy liberated by supernovae can have a profound impact on galaxy evolution, potentially heating significant amounts of gas and even ejecting it from a galaxy or host dark matter halo entirely. This is especially so at high redshift where haloes are on average less massive than in the local Universe, and possess correspondingly shallower potential wells. Supernovae also enrich the interstellar medium (ISM), altering the chemical composition of future stellar generations and changing the efficiency with which gas can cool (c.f. Equation 2).

2.5.1 Delayed supernova feedback

Many semi-analytic models make the simplifying assumption that all supernova feedback energy is released instantaneously, during the same snapshot in which the relevant stars formed. This approximation is motivated by the reasonable further assumption that the majority of supernova feedback energy is released by massive stars ($m_* > 8 M_{\odot}$) which have short ($\lesssim 40 \text{ Myr}$; [Portinari et al. 1998](#)) lifetimes, ending in violent SN-II. In the cases where the time span between each simulation snapshot is large (e.g. $\approx 250 \text{ Myr}$ in the case of the Millennium Simulation; [Springel et al. 2005](#)), the approximation of the instantaneous deposition of all supernova energy into the ISM is valid. However, motivated by the short dynamical time of systems at high redshift, the

separation between snapshots in our input simulation is approximately 11.1 Myr. It therefore takes at least three snapshots after a single coeval star formation episode for all stars more massive than $8M_{\odot}$ to have gone supernova. In order to accommodate this matching of time-scales in MERAXES, we have implemented a simple delayed supernova feedback scheme which we outline in this section.

We begin with the standard assumption that all supernova feedback energy is released by SN-II which are the end result of the evolution of stars with initial masses greater than $8M_{\odot}$. The basic methodology of our delayed feedback scheme is then to calculate the total amount of energy which should be injected into the ISM by a single star formation episode, and to release this energy gradually over time in proportion to the fraction of SN-II which will have occurred.

We assume a standard Salpeter (1955) initial mass function (IMF) with upper and lower mass limits of $0.1M_{\odot}$ and $120M_{\odot}$ respectively:

$$\phi(m) = \phi_{\text{norm}} m^{-2.35}, \quad (8)$$

where, by definition

$$\int_{0.1M_{\odot}}^{120M_{\odot}} m\phi(m) dm = 1, \quad (9)$$

and thus $\phi_{\text{norm}} = 0.1706$. With this choice of IMF, the number fraction of stars that will end their lives as type II supernovæ (η_{SNII}) is given by:

$$\eta_{\text{SNII}} = \int_{8M_{\odot}}^{120M_{\odot}} \phi(m) dm = 7.432 \times 10^{-3} M_{\odot}^{-1}. \quad (10)$$

If we further assume that each supernova produced injects a constant $E_{\text{nova}} = 10^{51}$ erg of energy into the ISM then, for a burst of mass Δm_* , the total amount of energy deposited into the ISM (ΔE_{total}) is

$$\Delta E_{\text{total}} = \epsilon_{\text{energy}} \Delta m_* \eta_{\text{SNII}} E_{\text{nova}}, \quad (11)$$

where ϵ_{energy} is a free parameter describing the efficiency with which the supernova energy couples to the surrounding gas. As is common practice, we model the mass of gas which is reheated by this energy deposition (Δm_{total}) as

$$\Delta m_{\text{total}} = \epsilon_{\text{mass}} \Delta m_*, \quad (12)$$

where ϵ_{mass} is a free parameter commonly referred to as the mass loading factor.

Croton et al. (2006) used constant values of ϵ_{energy} and ϵ_{mass} for all galaxies. However, we find that we are unable to replicate the observed shallow low-mass slope of the stellar mass function at $z \geq 5$ without adopting a value for these parameters that scale with mass. We therefore follow Guo et al. (2013) who encountered a similar issue (although at lower redshifts) leading them to adopt the following parametrizations for ϵ_{energy} :

$$\epsilon_{\text{energy}} = \alpha_{\text{energy}} \left[0.5 + \left(\frac{V_{\text{max}}}{V_{\text{energy}}} \right)^{-\beta_{\text{energy}}} \right], \quad (13)$$

and similarly for ϵ_{mass} :

$$\epsilon_{\text{mass}} = \min \left\{ \alpha_{\text{mass}} \left[0.5 + \left(\frac{V_{\text{max}}}{V_{\text{mass}}} \right)^{-\beta_{\text{mass}}} \right], \epsilon_{\text{mass}}^{\text{max}} \right\}, \quad (14)$$

where α_{energy} , V_{energy} , β_{energy} , α_{mass} , V_{mass} , and β_{mass} are all

free parameters. Since ϵ_{energy} corresponds to an efficiency, we enforce that it must take a value in the range 0–1 at all times. We have also imposed the additional constraint that the mass loading factor, ϵ_{mass} , cannot exceed an upper limit which we nominally set to be $\epsilon_{\text{mass}}^{\text{max}} = 10$ based on reasonable expectations for typical high- z galaxies (e.g. Martin 1999; Uhlir et al. 2012). For a standard energy-driven wind, $\beta_{\text{mass}} = 2$ (Murray et al. 2005). However, the value of β_{energy} is far less certain and depends on the poorly understood efficiency with which injected supernova energy is thermalized (Murray et al. 2005) and potential variations in the IMF of stars.

As discussed above, it takes approximately 40 Myr for an $8M_{\odot}$ star to go supernova (Portinari et al. 1998). As a result, the total amount of supernova energy released by a galaxy at any given snapshot, ΔE_{reheat} , will be dependent on the mass of stars formed both in the current and previous snapshots. We therefore explicitly track the total mass of stars formed in each galaxy (and all of its progenitors) for the last N_{SFH} snapshots². The value of N_{SFH} is dependent on the input N -body simulation and is chosen such that at least the last 40 Myr of star formation is recorded at all times. For *Tiamat* this corresponds to $N_{\text{SFH}} = 4$. At snapshot j , the value of ΔE_{reheat} is then

$$\Delta E_{\text{reheat},j} = \sum_{i=j-N_{\text{SFH}}}^{i=j} \frac{\Delta \eta_{i,j}}{\eta_{\text{SNII}}} \Delta E_{\text{total},i}. \quad (15)$$

Similarly, the amount of cold gas reheated by this energy is

$$\Delta m_{\text{reheat},j} = \sum_{i=j-N_{\text{SFH}}}^{i=j} \frac{\Delta \eta_{i,j}}{\eta_{\text{SNII}}} \Delta m_{\text{total},i}. \quad (16)$$

The term $\Delta \eta_{i,j}$ in the two equations above denotes the fraction of stars formed during snapshot i , that go supernova during snapshot j . This can be calculated by integrating the stellar IMF ($\phi(m)$) between suitably chosen mass limits:

$$\Delta \eta = \int_{m_{\text{low}}}^{m_{\text{high}}} \phi(m) dm. \quad (17)$$

The values of m_{high} and m_{low} are set by the range of stellar masses formed during snapshot i which will have had time to expend their fuel and go nova during the time spanned by snapshot j . To calculate these we use a functional form fit to the $Z=0.004$ H and He core burning lifetimes tabulated by Portinari et al. (1998), under the assumption that all stars go supernova immediately upon expending their H and He cores,

$$\log_{10}(m(t)) = \frac{a}{\log_{10}(t/\text{Myr})} + b \exp\left(\frac{c}{\log_{10}(t/\text{Myr})}\right) + d, \quad (18)$$

where $(a, b, c, d) = (0.7473, -2.6979, -4.7659, 0.5934)$ and t is the time since the stars formed. This fit is accurate to within 6% for all values of t appropriate for this work. For simplicity, we also approximate the star formation which occurs during any given snapshot by a single coeval burst at the middle of that snapshot. Although crude, this approximation results in an error of at most $\approx 15\%$ in $\Delta \eta$ which rapidly becomes negligible as the time since the burst increases (i.e. $j-i$ increases). Finally we note that since we are assuming that all supernova feedback energy is produced by SN-II,

² SFH \rightarrow star formation history

we enforce a minimum m_{low} value of $8M_{\odot}$ when evaluating Equations 15 & 16 above.

The eventual fate of the reheated material depends on both its mass, m_{reheat} , and the amount of energy injected, ΔE_{reheat} . If we assume the gas to be adiabatically heated to the virial temperature of its host halo, the associated change in thermal energy is given by:

$$\Delta E_{\text{hot}} = 0.5 \Delta m_{\text{reheat}} V_{\text{vir}}^2 . \quad (19)$$

If $\Delta E_{\text{reheat}} \geq \Delta E_{\text{hot}}$ then there is more energy injected into the reheated gas than is required to raise it to the virial temperature of the halo. We therefore assume the gas to be added to the hot halo of the host FoF group. Any excess energy is assumed to then go into ejecting some fraction of the FoF group hot reservoir from the system entirely:

$$\Delta m_{\text{eject}} = \frac{\Delta E_{\text{reheat}} - \Delta E_{\text{hot}}}{0.5 m_{\text{hot}} V_{\text{vir}}^2} m_{\text{hot}} , \quad (20)$$

where V_{vir} is the virial velocity of the FoF group. If instead $\Delta E_{\text{reheat}} < \Delta E_{\text{hot}}$, only an energetically feasible fraction of the total reheated mass is added to the FoF group hot reservoir:

$$\Delta m_{\text{hot}} = \frac{\Delta E_{\text{reheat}}}{0.5 V_{\text{vir}}^2} , \quad (21)$$

with the rest raining back down to the galaxy in a galactic fountain.

Any gas and metals which are successfully expelled from the system entirely are placed into a separate ‘ejected’ reservoir. Here they are assumed to play no further role in the evolution of the galaxies in the host FoF group until the group falls into a more massive system. At this point, the ejected material is assumed to be re-accreted into the new group and is added to its hot halo component.

2.5.2 Delayed versus contemporaneous feedback

In practice, we apply our supernova scheme in two phases. First, the amount of mass reheated and ejected due to past star formation episodes is calculated as described above. After the masses of the various baryonic reserves have been appropriately updated, the amount of new star formation in the current snapshot is then determined (cf. Section 2.4). In this way, ongoing energy injection from past star formation episodes is able to prevent new stars from forming in the current time step altogether.

After calculating the mass of stars formed, the corresponding reheated and ejected masses due to any stars with short enough lifetimes to go nova in the current time step are also calculated. If the total amount of cold gas removed from the galaxy due to both star formation and the corresponding contemporaneous supernova feedback exceeds that which is available, the mass of stars formed in the current time step is reduced until consistency is achieved.

2.6 Metal enrichment

As is common in semi-analytic models (e.g. De Lucia et al. 2004; Somerville et al. 2008; Guo et al. 2011), we implement a simple metal enrichment scheme whereby a fixed yield, Y , of metals is released into the ISM per unit mass

of stars formed. Again, we assume that these metals are released predominantly by massive stars which end their lives as SN-II and we gradually release them over time as these supernovae occur. However, since a more massive star will generally release more metals during its lifetime than a less massive counterpart, we release these metals in proportion to the mass fraction of SN-II (as opposed to the number fraction as was used above). In other words

$$\Delta m_{Z,j} = \sum_{i=j-N_{\text{SFH}}}^{i=j} \frac{\Delta m_{\text{SN};i,j} Y \Delta m_{*}}{m_{\text{SNII}}} , \quad (22)$$

where $m_{Z,j}$ is the mass of metals released during snapshot j , m_{SNII} is the total fraction of stars with initial masses greater than $8M_{\odot}$, and $\Delta m_{\text{SN};i,j}$ is the fraction of stars formed during snapshot i that go nova during snapshot j .

Analogous to Equations 10 and 17 above, m_{SN} and Δm_{SN} are given by

$$m_{\text{SNII}} = \int_{8M_{\odot}}^{120M_{\odot}} m \phi(m) dm = 0.144 , \quad (23)$$

$$\Delta m_{\text{SN}} = \int_{m_{\text{low}}}^{m_{\text{high}}} m \phi(m) dm , \quad (24)$$

where m_{high} and m_{low} are as defined in Section 2.5.

The metals released into the ISM in this manner are assumed to be uniformly mixed with the cold gas of the galaxy. From here they can be further distributed to the hot halo or ejected from the system entirely via supernova feedback. Metals which do end up in the hot gas reservoir can then enhance the cooling rate of gas on to the galaxy through metal line emission (see Equation 2).

2.7 Stellar mass recycling

A common assumption of many semi-analytic models is the so-called instantaneous recycling approximation (IRA), in which some fixed fraction of the stellar mass formed during each time step is instantaneously recycled back into the ISM. The precise value of this fraction varies from model to model and is often left as a free parameter; however, most works employ a value of approximately 30–40% (e.g. Cole et al. 2000; Croton et al. 2006; Somerville et al. 2008; Henriques et al. 2015).

Given our choice of IMF (see Section 2.5), a recycle fraction of 40% corresponds to all stars more massive than approximately $1M_{\odot}$ instantaneously going supernova. However, the lifetime of a $1M_{\odot}$ star is close to the current age of the Universe (e.g. Portinari et al. 1998) and hence the IRA can only be considered valid for galaxies around $z=0$ (i.e. well past the peak of the Universal star formation rate density). At $z \gtrsim 2$, where the majority of galaxies have stellar populations dominated by recent star formation, this approximation becomes invalid and we are forced to consider a more realistic alternative.

Our stellar mass recycling prescription is divided into two parts:

(i) When implementing our delayed supernova feedback prescription, we assume that the initial stellar mass of all supernovae is returned to the cold gas reservoir of the galaxy (thus ignoring any mass that may be locked up in long lived remnants such as neutron stars and black holes).

(ii) As discussed in Section 2.5, we explicitly track the star formation history of each galaxy for the last N_{SFH} snapshots. In order to calculate the recycled mass from older stars we approximate these as having formed in a single coeval burst which occurred at a time defined by their mass-weighted age. Equation 24 then allows us to calculate the relevant mass of stars which would have gone nova and this is again assumed to be returned the cold ISM in its entirety. Although crude, the approximation of a single coeval burst for all older stars provides the correct stellar mass loss to within less than 5% error at all times³ given the snapshot cadence of *Tiamat* and our fiducial value of $N_{\text{SFH}}=4$.

2.8 Halo infall and gas stripping

As haloes inspiral towards more massive systems, tidal forces experienced during repeated pericentric passages can lead to the stripping of loosely bound material from the outer regions. In MERAXES, if the mass of an FoF group drops, then a pro rata fraction of the ejected and/or hot baryonic content of the halo is also removed. In practice, the amount of mass which must be removed is given by the value of m_{infall} (as defined in Equation 1) which will be negative in such systems. This material is taken first from the ejected reservoir, with further mass being removed from the hot halo component if required. No baryons are ever taken from the cold gas or stellar mass reservoirs as these are assumed to be protected from such tidal losses by their position deep in the central potential well of their haloes.

Further to these long-range tidal forces, galaxies infalling into groups or clusters are observed to be subjected to a number of dynamical processes which remove gas from the outskirts of the system, including ram-pressure stripping, strangulation, and harassment (e.g. van den Bosch et al. 2008; Peng et al. 2015). We model the combined effects of these processes by assuming that all FoF groups are instantly stripped of their entire hot and ejected gas reservoirs upon infall into a more massive structure, with their combined mass and metals being added to the hot component of the new parent. Although such a rapid stripping represents the most extreme scenario possible, we note that this approximation has been made in a number of previous semi-analytic models and defer an improved and more realistic treatment to future works.

2.9 Mergers

Mergers play an important role in the build up of galaxy stellar mass, both through hierarchical mass assembly and induced star formation. This is particularly so at high- z where their prevalence is enhanced (cf. Paper I). In MERAXES (as in almost all semi-analytic models) these galaxy merger events are triggered by the merging of the corresponding host dark matter haloes. Following Croton et al. (2006), when a dark matter halo is marked as having merged, we utilize dynamical friction arguments to approximate the time taken for the

orbit of the incoming galaxy to decay and the corresponding galaxy–galaxy merger to occur (Binney & Tremaine 2008):

$$t_{\text{merge}} = \alpha_{\text{merge}} \frac{V_{\text{vir}} r_{\text{gal}}^2}{G m_{\text{gal}} \ln(1 + M_{\text{vir}}/m_{\text{gal}})}, \quad (25)$$

where it is standard to take $\alpha_{\text{merge}}=1.17$, r_{gal} is the distance between the most-bound particle of the parent and the infalling halo, m_{gal} is the total mass of the infalling galaxy, and M_{vir} and V_{vir} are the virial properties of the parent. In MERAXES, all of these quantities are evaluated at the last time the infalling halo was successfully identified in the trees.

The value of $\alpha_{\text{merge}}=1.17$ is based on the assumption that t_{merge} is calculated at the moment the infalling halo crosses the virial radius of the parent. However, we instead calculate t_{merge} at the time at which the infalling halo can no longer be identified in the *Tiamat* simulation and is thus marked as having merged in our input merger trees. This results in an overestimate of the merger time-scale which worsens the longer the infalling halo remains identified after crossing the virial radius of the parent (e.g. Hopkins et al. 2010). Even in dense environments, the accurate merger trees produced from *Tiamat* results in haloes being identified for extended periods before the merger event occurs. Furthermore, previous authors have found that changes to the value of α_{merge} have been necessary in order to match observational constraints on the luminous end of the galaxy luminosity function (De Lucia & Blaizot 2007) and idealized N -body halo merger simulations (e.g. Boylan-Kolchin et al. 2008). On average, we find that infalling haloes are successfully tracked in our input merger trees until $r_{\text{gal}} \approx 0.7 R_{\text{vir}}$, with a weak trend to be identified to smaller fractional radii with increasing redshift. Noting that $t_{\text{merge}} \propto r_{\text{gal}}^2$, we therefore choose to fix $\alpha_{\text{merge}}=0.5$. We also note that if, after starting the merger clock, the parent galaxy itself experiences a merger, then we assume that all of its infalling galaxies also undergo a merger with the same target.

Galaxy mergers can drive strong shocks and turbulence in any participating cold gas, driving this material towards the inner regions of the parent galaxy and resulting in an efficient burst of star formation. We model the fraction of cold gas consumed by such a burst, e_{burst} , using the prescription introduced by Somerville et al. (2001):

$$e_{\text{burst}} = \alpha_{\text{burst}} (m_{\text{gal}}/m_{\text{parent}})^{\gamma_{\text{burst}}}, \quad (26)$$

where m_{gal} and m_{parent} are the corresponding baryonic masses (i.e. cold gas + stellar mass), and we follow Croton et al. (2006) by setting the parameters $\alpha_{\text{burst}}=0.56$ and $\gamma_{\text{burst}}=0.7$. This relation agrees well with the results of numerical simulations of mergers with baryonic mass ratios in the range 0.1–1.0 (Cox et al. 2004). For merger events where the mass ratio is less than 0.1, we suppress any merger-driven star formation.

For simplicity, we assume that all of the stars formed in a merger-driven burst do so within a single snapshot. At $z \sim 8$, the median dynamical time of a galaxy disc in MERAXES is $\sim 60\%$ of the time between two consecutive snapshots of *Tiamat* (~ 11.2 Myr). Hence, this approximation is roughly equivalent to the assumption that the merger-driven burst occurs on a time-scale approximately less than one disc dynamical time for the majority of galaxies. Although the disc dynamical time does increase with decreasing redshift, by $z \sim 5$ the median is still only equal to one snapshot and

³ This has been confirmed by tests we have performed using a number of idealized star formation histories (exponentially increasing, exponentially decreasing, constant, multiple burst, and random).

hence this approximation remains valid for the majority of galaxies.

2.10 Ghost galaxy evolution

A ghost dark matter halo is one which is temporarily unresolved in our input merger trees. This can be due to a number of reasons, but is most commonly a result of a smaller halo passing through or nearby a much more massive structure. The *Tiamat* merger trees used in this work are carefully constructed to identify these artefacts, resulting in the skipping of a potentially large number of snapshots between haloes and their descendants. In many semi-analytic models, the galaxies hosted by such haloes are simply ignored until their halo is later re-identified. In some cases, re-identification fails or is not even attempted, resulting in spurious galaxy merger and creation events. However, we must ensure that we correctly include these objects at all snapshots in order to account for their ionizing photon contribution.

Due to the lack of knowledge of the properties of a ghost’s host dark matter halo, we are unable to implement many of the physics prescriptions outlined above. We therefore simply allow these galaxies to passively evolve during the time over which they are identified as ghosts, forming no new stars but experiencing the delayed supernova feedback from previously formed generations. When the host halo is eventually re-identified, we assume that any associated star formation occurred in a single coeval burst at $0.5\Delta t$, where Δt is the time since the halo was last identified. We then back-fill the stellar mass history appropriately for use in our delayed supernova feedback scheme.

2.11 Reionization

A key goal of DRAGONS is to connect the evolution of the 21 cm reionization structure to the formation of the source galaxy population. As such, MERAXES has been developed to be the first semi-analytic galaxy formation model to fully and self-consistently couple the process of reionization (in particular, the presence of a photo dissociating UVB) to the evolution of galaxies both temporally and spatially. To achieve this we have embedded a specially modified version of the semi-numerical reionization code, 21CMFAST (Mesinger et al. 2011), that includes the calculation of the local ionizing UVB described by Sobacchi & Mesinger (2013) and, importantly, makes full use of the realistic galaxy properties provided by MERAXES.

2.11.1 Self-consistent reionization with 21CMFAST

The basic methodology of 21CMFAST is to use an excursion set formalism in order to identify ionized bubbles where the integrated number of ionizing photons is greater than the number of absorbing atoms and associated recombinations:

$$N_{b*}(r)N_{\gamma}f_{\text{esc}} \geq (1 + \bar{N}_{\text{rec}})N_{\text{atom}}(r). \quad (27)$$

Here $N_{\text{atom}}(r)$ is the integrated number of atoms being ionized within a sphere of radius r , $N_{b*}(r)$ is the number of stellar baryons in the same volume, N_{γ} is the mean number of ionizing photons produced per stellar baryon, f_{esc} is

the escape fraction of these photons, and \bar{N}_{rec} is the mean number of recombinations per baryon. If we assume that helium is singly ionized at the same rate as cosmic hydrogen, then expanding Equation 27 in terms of the integrated stellar ($m_*(r)$) and total ($M_{\text{tot}}(r)$) masses within r gives

$$\frac{m_*(r)}{m_{\text{p}}}N_{\gamma}f_{\text{esc}} \geq (1 + \bar{N}_{\text{rec}})\frac{f_{\text{b}}(1 - \frac{3}{4}Y_{\text{He}})M_{\text{tot}}(r)}{m_{\text{p}}}, \quad (28)$$

where Y_{He} is the helium mass fraction, m_{p} is the proton mass, and the term $(1 - \frac{3}{4}Y_{\text{He}})$ corresponds to the combined number of hydrogen and helium atoms per baryon.

It is common for Equation 28 to be re-written in terms of an H II ionizing efficiency, ξ :

$$\xi \frac{m_*(r)}{M_{\text{tot}}(r)} \geq 1, \quad (29)$$

where

$$\xi = 6214 \left(\frac{0.157}{f_{\text{b}}}\right) \left(\frac{N_{\gamma}}{4000}\right) \left(\frac{f_{\text{esc}}}{0.2}\right) \left(\frac{0.82}{1 - \frac{3}{4}Y_{\text{He}}}\right), \quad (30)$$

and we have excluded the $1 + \bar{N}_{\text{rec}}$ term based on studies of the high-redshift Lyman- α forest which suggest $\bar{N}_{\text{rec}} \sim 0$ in the diffuse IGM (e.g. Bolton & Haehnelt 2007; McQuinn et al. 2011). Despite this simplifying assumption of $\bar{N}_{\text{rec}} = 0$, we note that we implicitly include a mean-free path of ionizing photons through the IGM in our calculation by starting our excursion set calculation at an appropriate scale (Sobacchi & Mesinger 2013). The right-hand side of this equation includes our fiducial values for each of the physical variables. The number of ionizing photons per stellar baryon, N_{γ} , is set by the assumed stellar IMF whilst both f_{b} and Y_{He} are well constrained by cosmology. Of all of these terms, only f_{esc} is poorly known for high-redshift galaxies (Wise & Cen 2009; Raćević et al. 2011; Kuhlen & Faucher-Giguère 2012, e.g.). Our fiducial value of 0.2 is primarily chosen to provide a reionization history which is consistent with the latest *Planck* 2015 electron scattering optical depth measurements (Planck Collaboration 2015, see Section 3 below).

By applying our integrated 21CMFAST algorithm to grids of stellar and total mass within MERAXES we can use Equation 29 to produce a neutral hydrogen fraction (x_{HI}) grid for the entire simulation volume. In order to then determine how this spatially and temporally evolving ionization structure affects the baryon fraction modifier, f_{mod} , of individual FoF groups we utilize the UVB feedback model of Sobacchi & Mesinger (2013). Using idealized 1D hydrodynamical simulations of a static, uniform ionizing UVB impinging on collapsing dark matter haloes, Sobacchi & Mesinger (2013) found that f_{mod} was well described by

$$f_{\text{mod}} = 2^{-M_{\text{filt}}/M_{\text{vir}}}, \quad (31)$$

where M_{vir} is the mass of the halo and M_{filt} is the ‘filtering mass’ representing the mass at which $f_{\text{mod}} = 0.5$:

$$M_{\text{filt}} = M_0 J_{21}^a \left(\frac{1+z}{10}\right)^b \left[1 - \left(\frac{1+z}{1+z_{\text{ion}}}\right)^c\right]^d. \quad (32)$$

Here z_{ion} is the redshift at which the collapsing halo was first exposed to the UVB and the parameters $(M_0, a, b, c, d) = (2.8 \times 10^9 M_{\odot}, 0.17, -2.1, 2.0, 2.5)$ were found by the authors

to provide the best fit to their results. The J_{21} term represents the local UVB intensity:

$$J(\nu) = J_{21} \left(\frac{\nu}{3.2872 \times 10^{15} \text{ Hz}} \right)^{-\alpha} \times 10^{-21} \text{ erg s}^{-1} \text{ Hz}^{-1} (\text{proper cm})^{-2} \text{ sr}^{-1}, \quad (33)$$

where $\alpha = 5.0$ for a stellar-driven UV spectrum (Thoul & Weinberg 1996).

In order to calculate f_{mod} using this formalism, we need to know both the redshift at which the IGM surrounding each halo was first ionized, z_{ion} , and the local ionizing background intensity at this time, J_{21} . The average UVB intensity which a galaxy is exposed to within an ionized region, \bar{J}_{21} , is given by

$$\bar{J}_{21} = \frac{(1+z)^2}{4\pi} \lambda_{\text{mfp}} h \alpha f_{\text{bias}} \bar{\epsilon}, \quad (34)$$

where λ_{mfp} is the comoving mean-free path of ionizing photons (which is assumed here to be equal to the radius of the ionized bubble, r) and h is the Planck constant. The term $f_{\text{bias}}=2$ is introduced to account for the effect of galaxy clustering on boosting the ionizing emissivity at halo locations relative to the spatial average (Mesinger & Dijkstra 2008). The term $\bar{\epsilon}$ represents the ionizing emissivity, the time-averaged number of ionizing photons emitted into the IGM per unit time, per unit comoving volume. Approximating the average rate of stellar mass growth of all galaxies within this region as $m_{*,\text{gross}}(r)/t_{\text{H}}$, where $m_{*,\text{gross}}(r)$ is the gross stellar mass formed within r (i.e. without any decrement due to stellar evolution) and t_{H} is the Hubble time, $\bar{\epsilon}$ can be expressed as

$$\bar{\epsilon} = \frac{f_{\text{esc}} N_{\gamma}}{\frac{4}{3} \pi r^3 m_{\text{p}}} \frac{m_{*,\text{gross}}(r)}{t_{\text{H}}}. \quad (35)$$

Our utilization of $m_{*,\text{gross}}(r)/t_{\text{H}}$, instead of the true instantaneous star formation rate predicted by MERAXES, is motivated by the need to smooth out the often bursty star formation histories of our galaxies. The filtering mass formula of Equation 32 assumes that the ionizing background intensity within a cell remains constant with time. This is a reasonable approximation due to the weak sensitivity of M_{filt} on the UVB intensity ($M_{\text{filt}} \propto J_{21}^{0.17}$). Sobacchi & Mesinger (2013) also find that the \bar{J}_{21} remains approximately constant within H II regions, further validating this approximation. However, fixing the UVB intensity at the snapshot of ionization results in smaller bubbles having artificially high or low \bar{J}_{21} values depending on the current star forming state of the source galaxies. This introduces artificial scatter into the calculation which can become important when comparing the effect of reionization on the evolution of individual galaxies (see Section 4.5).

In practice, the coupling between galaxy evolution and reionization within MERAXES is implemented as follows.

(i) For a single time step in the simulation, MERAXES evolves all of the galaxies in the entire *Tiamat* volume.

(ii) Our 21cmFAST algorithm constructs and processes halo mass, stellar mass, and averaged star formation rate grids, along with pre-computed total matter density grids. For this work, and all of the results herein, we use a grid resolution of 512^3 . After applying the excursion set formalism and equations outlined above, a grid of \bar{J}_{21} and x_{HI} values is generated.

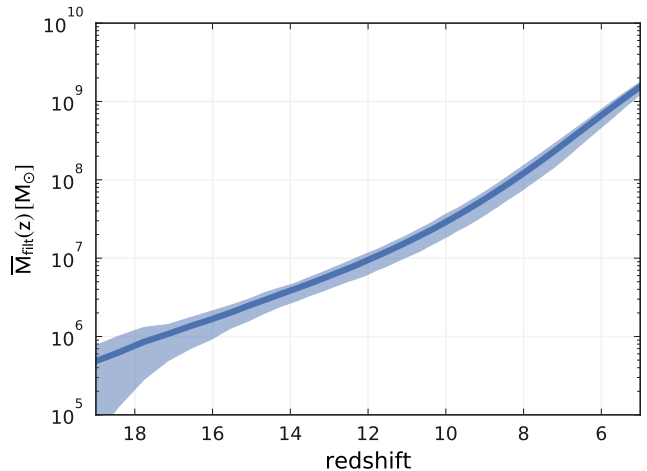


Figure 1. The mean filtering mass, \bar{M}_{filt} , of FoF groups in the fiducial patchy reionization model as a function of redshift. For our homogeneous comparison model, these filtering mass values are applied to every FoF group in the simulation, regardless of their environment or local reionization history, thus allowing us to directly assess the effect of ignoring this information as is commonly done in traditional semi-analytic galaxy formation models. The blue shaded region indicates the 68% confidence intervals calculated using the spatial variation in the mean from 125 non-overlapping subvolumes comprising the full simulation.

(iii) Using the x_{HI} grid, MERAXES keeps track of the redshift at which each cell first became ionized (z_{ion}) and the corresponding \bar{J}_{21} . It then calculates the baryon fraction modifier of each grid cell following Equation 31.

(iv) In order to calculate the amount of freshly infalling baryonic material it should accrete, each FoF group uses the baryon fraction modifier of the grid cell in which it is located in the following simulation time step (see Section 2.2 above).

(v) This process is then repeated for each of the time steps (of which there are 100 for our input simulation, *Tiamat*, between $5 < z < 35$).

Through this procedure, the evolution of galaxies and reionization in the simulation are self-consistently coupled both temporally and spatially.

2.11.2 Homogeneous model

For comparison, we also employ a ‘homogeneous’ reionization prescription using M_{filt} values that depend on redshift alone (i.e. no information about the spatial distribution of the IGM ionization state is required). Prescriptions such as this (e.g. Gnedin 2000; Kravtsov et al. 2004) have been commonly employed by semi-analytic models for many years (e.g. Benson et al. 2002; De Lucia & Blaizot 2007; Somerville et al. 2008).

At each time step in the simulation, we use our fiducial patchy reionization prescription described above to calculate the number-weighted mean filtering mass of all FoF groups in the volume. We then re-run MERAXES, applying this redshift dependent \bar{M}_{filt} value to all FoF groups when calculating their baryon fraction modifier as per Equation 31. By generating $\bar{M}_{\text{filt}}(z)$ from our fiducial model in this way, we are able to use the homogeneous model result as a baseline with

which to assess the detailed effects of a self-consistent, spatially dependent reionization prescription on the evolution of the source galaxy population, whilst simultaneously providing a useful filtering mass relation for $z \leq 5$, that can be applied quickly and easily. In Fig. 1, we show the evolution of \bar{M}_{fit} . The blue shaded region indicates the 68% confidence intervals calculated using the spatial variation of the mean in 125 subvolumes. The evolution in the filtering mass is well approximated by the following functional form:

$$\log_{10}(\bar{M}_{\text{fit}}(z)/M_{\odot}) = \theta_1 \exp(\theta_2 z) + \theta_3, \quad (36)$$

where $\theta_1 = 7.51_{-0.18}^{+0.26}$, $\theta_2 = -0.090_{-0.01}^{+0.01}$ and $\theta_3 = 5.59_{-0.43}^{+0.35}$. The fitted parameter values were calculated using Markov chain Monte Carlo (MCMC) methods with a standard chi-squared likelihood, and provide a fit which is accurate to within $\sim 2\%$ of the mean model result across all redshifts. As we will demonstrate in Section 4, our homogeneous prescription does a reasonable job of reproducing the mean evolution of the stellar mass functions and global neutral fractions predicted by the full, patchy reionization implementation.

3 MODEL CALIBRATION

The free parameters of the model were manually calibrated (by hand) to replicate the observed evolution of the galaxy stellar mass function between redshifts 5 and 7, as well as the integrated free electron Thomson scattering optical depth measurements. The evolution of the stellar mass function has been shown by previous statistical investigations of semi-analytic models to provide a tight constraint on both the star formation efficiency and supernova feedback parameters (e.g. Henriques et al. 2013; Mutch et al. 2013). By combining this with the Thomson scattering optical observations, we can additionally put constraints on the escape fraction of ionizing photons (f_{esc}), and thus all of the free parameters of our model, as listed in Table 1.

It could be argued that the luminosity function would provide a more fundamental constraint on the model, rather than the stellar mass function. However, whilst it is true that converting observed galaxy luminosities to stellar masses involves a number of assumptions and potentially unreliable conversions, the same is also true for the inverse procedure of converting model stellar masses to luminosities. Stellar masses are intrinsic predictions of semi-analytic models, whilst luminosities require an extra layer of modelling. For example, changing the IMF has a relatively small impact on the stellar masses predicted by the model, but can have a significant impact on the resulting luminosity function. In order to accurately model luminosities in various bands, one must typically calculate a full spectral energy distribution (SED) for every object, applying model-dependent Lyman α absorption, sample selection (e.g. in colour–colour space), and poorly understood dust corrections. Furthermore, doing this for all galaxies at multiple redshifts can take a significant amount of time and memory which prohibits its usefulness when running a model many times for calibration purposes.

The redshift range $5 \leq z \leq 7$ corresponds to the highest redshifts for which reliable observed stellar mass functions are available. In particular, we make use of the mass functions estimated by González et al. (2011), Duncan et al. (2014), Grazian et al. (2015), and Song et al. (2016). Both

Duncan et al. (2014) and Grazian et al. (2015) utilize data collected from the Cosmic Assembly Near-infrared Deep Extragalactic Survey (CANDELS; Grogin et al. 2011; Koekoer et al. 2011) GOODS South field with stellar masses directly obtained from SED fitting of combined optical and near-infrared space-based observations, and include the effects of both nebular line and continuum emission. In addition, Grazian et al. (2015) include a detailed treatment of the effects of Eddington bias (Eddington 1913) on the normalization and slope of their derived mass functions. Whilst Song et al. (2016) also utilize CANDELS infrared data, they instead carry out a hybrid SED stacking technique to derive a redshift dependent stellar mass–UV luminosity relation which is then combined with measured UV luminosity functions to estimate the galaxy stellar mass function. Similarly, González et al. (2011) utilized data combined from *Hubble Space Telescope* and *Spitzer* observations, but with stellar masses obtained via mass–UV luminosity relations calibrated at $z=4$ alone.

In addition to the stellar mass function which constrains the integrated amount of star formation driving reionization, the corresponding ionizing photon budget is also set by the escape fraction. One of the primary observational constraints on the timing and duration of reionization comes from the measured integrated optical depth to Thomson scattering of cosmic microwave background photons by free electrons, τ_e :

$$\tau_e = \int_{z=0}^{\infty} \frac{cdt}{dz} (1+z)^3 \sigma_{\text{T}} \times [Q_{\text{HII}}^{\text{m}} \langle n_{\text{H}} \rangle + (Q_{\text{HeII}}^{\text{m}} + 2Q_{\text{HeIII}}^{\text{m}}) \langle n_{\text{He}} \rangle] dz, \quad (37)$$

where $\sigma_{\text{T}} = 6.652 \times 10^{-25} \text{ cm}^2$ is the Thomson scattering cross-section, Q_X^{m} is the mass-weighted global ionized fraction of species X , and $\langle n_{\text{H}} \rangle = 1.88 \times 10^{-7} (\Omega_{\text{b}} h^2 / 0.022) \text{ cm}^{-3}$ and $\langle n_{\text{He}} \rangle = 0.148 \times 10^{-7} (\Omega_{\text{b}} h^2 / 0.022) \text{ cm}^{-3}$ are the average comoving density of hydrogen and helium, respectively (Wyithe & Loeb 2003). For this work, we have assumed that helium is singly ionized at the same rate as hydrogen (i.e. $Q_{\text{HeII}}^{\text{m}}(z) = Q_{\text{HII}}^{\text{m}}(z)$) and only becomes doubly ionized at $z=4$ (i.e. $Q_{\text{HeIII}}^{\text{m}} = 1.0$ or 0 for z greater than or less than 4 respectively; e.g. Kuhlen & Faucher-Giguère 2012). As we shall demonstrate in the following sections, τ_e primarily constrains the escape fraction of ionizing photons, f_{esc} , in the model.

The resulting parameter values for our fiducial model constrained against both the high- z stellar mass function evolution and integrated electron scattering optical depth are presented in Table 1. It is important to note that, although these parameter values provide a good match to the constraining observations and are broadly consistent with comparable works where appropriate (see second-to-last column), they may not be the only possible solution. However, through testing extreme (to the point of being physically implausible) parameter combinations we are able to ascertain that supernova feedback is the only feedback mechanism in our model capable of producing a stellar mass function with a slope consistent with observations. Regardless, we impress upon the reader that all of the results in this work must be interpreted within the context of these particular chosen parameter values alone. In future work we will carry out a full MCMC analysis to accurately constrain the free model parameters against a wider range of observational quantities

Table 1. The fiducial parameter values used throughout this work. Values were constrained to visually reproduce the observed evolution in the galaxy stellar mass function between $z=5$ and 7 (see Fig. 2). The quoted *Munich* model values represent the range of fiducial values utilized in the following works (where appropriate): Croton et al. (2006), Guo et al. (2011, 2013), Mutch et al. (2013), and Henriques et al. (2013, 2015). All of the parameters in these works were calibrated against $z<3$ observations. However, they are presented here as a rough guide to the range of plausible values.

Parameter	Prescription	Equation	Description	<i>Munich</i> model values	Fiducial value
Σ_{norm}	Star formation (§2.4)	5	Critical cold gas surface density normalization	0.26–0.38	0.2
α_{SF}	–	7	Star formation efficiency	0.01–0.07	0.03
α_{energy}	Supernova feedback (§2.5)	13	Energy coupling efficiency normalization	0.18–0.7	0.5
β_{energy}	–	13	Coupling efficiency V_{max} scaling	0–3.5	2.0
V_{energy}	–	13	Coupling efficiency V_{max} normalization	70–336	70.0
α_{mass}	–	14	Mass loading normalization	2.1–10.3	6.0
β_{mass}	–	14	Mass loading V_{max} scaling	0–3.5	0.0
V_{mass}	–	14	Mass loading V_{max} normalization	70–430	70.0
$\epsilon_{\text{mass}}^{\text{max}}$	–	14	Maximum mass loading value	–	10.0
Y	Metal enrichment (§2.6)	22	Mass of metals per unit mass of SN	0.03–0.047	0.03
f_{esc}	Reionization (§2.11)	30	Ionizing photon escape fraction	–	0.2

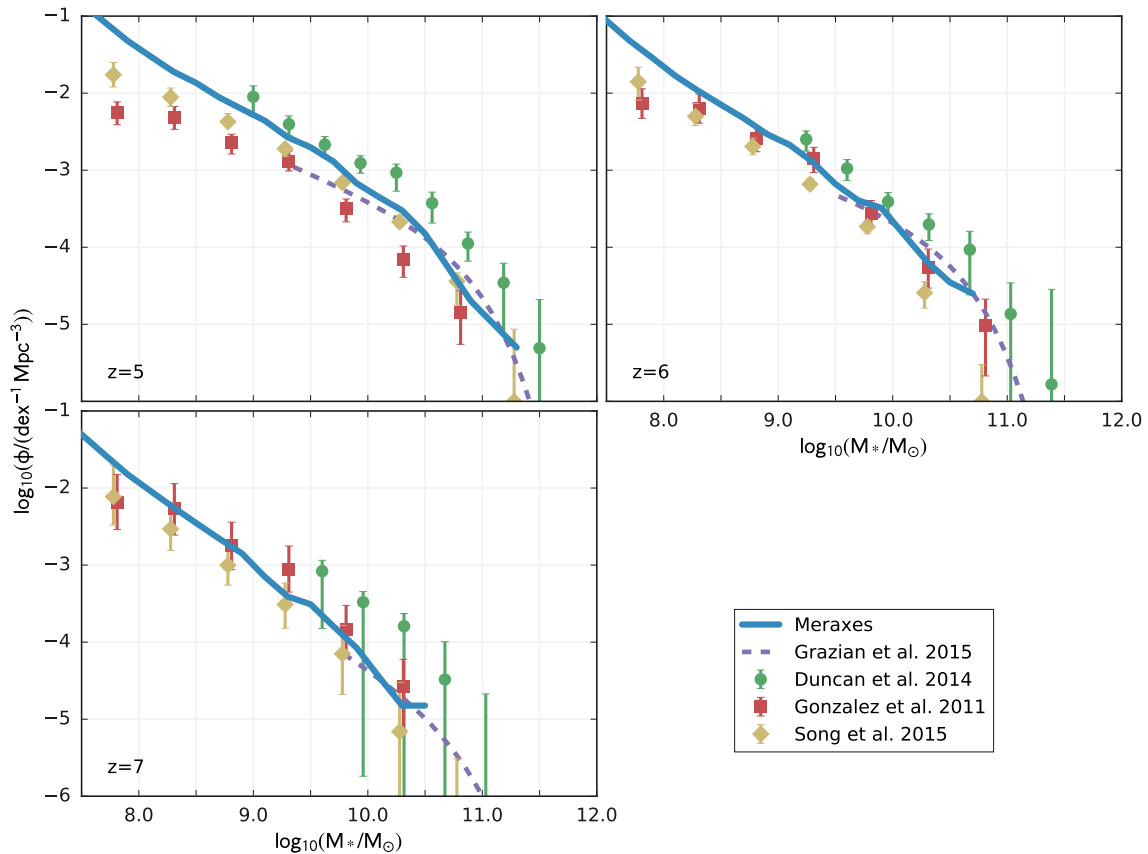


Figure 2. The evolution of the galaxy stellar mass function from $z=5-7$. Coupled with the measured Thomson scattering optical depth (see Fig. 4), these are the only observational constraints applied to MERAXES throughout this work unless explicitly stated. Data points show the observations of Duncan et al. (2014), González et al. (2011) and Song et al. (2016). The purple dashed lines show the best-fitting Schechter functions of Grazian et al. (2015). Solid blue lines show the self-consistent patchy reionization model using our fiducial parameter values. Best fit low-mass slopes are provided in Table 2. All observations have been corrected to a Salpeter IMF where necessary.

as well as explore any degeneracies which may exist between them (e.g. Lu et al. 2011b; Mutch et al. 2013).

In Fig. 2 we present the fiducial model stellar mass functions (blue solid lines) along with the constraining observations. All observations have been converted to a Salpeter IMF and $h=0.678$ where necessary. The error bars on observed data points include contributions from Poisson noise and uncertainties in photometric redshift determinations. However, they neglect the systematic uncertainties associated with the estimation of stellar masses from photometric data (e.g. stellar population synthesis model variations, and photometric uncertainties).

We are able to achieve an excellent match to the normalization, shape, and evolution of the observed mass function across all plotted redshifts. At $z=5$, where there is the largest divergence between different observational data sets, we chose parameter values which provided a reasonable compromise between each. However, at the low-mass end we have chosen to follow the observations of Duncan et al. (2014) as they use a large data set with stellar masses obtained from SED fitting and provide actual data points rather than a Schechter fit. The quality of the agreement between our model and the observational data gives us faith that our implemented physical prescriptions are both reasonable and applicable at the high redshifts of interest in this work.

Although typically producing fewer ionizing photons than their more massive counterparts, low mass galaxies with $M < M_*$ are expected to contribute a large fraction of the overall ionizing photon budget due to their high number density. For this reason, the low-mass slope of the stellar mass function, α , is of particular importance to reionization. In Table 2, we provide the MERAXES best-fit α parameters at each redshift, obtained by fitting a standard Schechter function to the model results using MCMC methods⁴ and are in good statistical agreement with the corresponding values found by Duncan et al. (2014) of $-1.90^{+0.21}_{-0.16}$, $-1.91^{+0.91}_{-0.59}$ and $-2.31^{+1.31}_{-0.19}$ for redshifts 5, 6 and 7 respectively.

In the top panel of Fig. 3 we present the $z=5$ distribution of total stellar mass (i.e. summed over all galaxies) in each FoF group as a function of the group virial mass in our fiducial model. The median relation (solid black line) is well described by a power law with a slope of ~ 1.4 . This shows good agreement with simple energy conservation arguments which suggest a slope of ~ 1.7 for supernova feedback-regulated galaxy growth and a fixed cold gas mass fraction (Wyithe & Loeb 2013). However, at FoF group masses below $M_{\text{vir}} \approx 10^{9.5} M_{\odot}$ there is a rapid increase in the spread of stellar mass values. This is due to a combination of supernova and reionization feedback effects, as well as a low star formation efficiency in these small, often diffuse haloes. In the lower panel of Fig. 3 we show the evolution of the median FoF group M_*-M_{vir} relation as a function of redshift. Interestingly, there is no statistically significant evolution in either the slope or normalization of the relation with redshift. However, the same simple energy conservation arguments which provided a good agreement for the slope of the

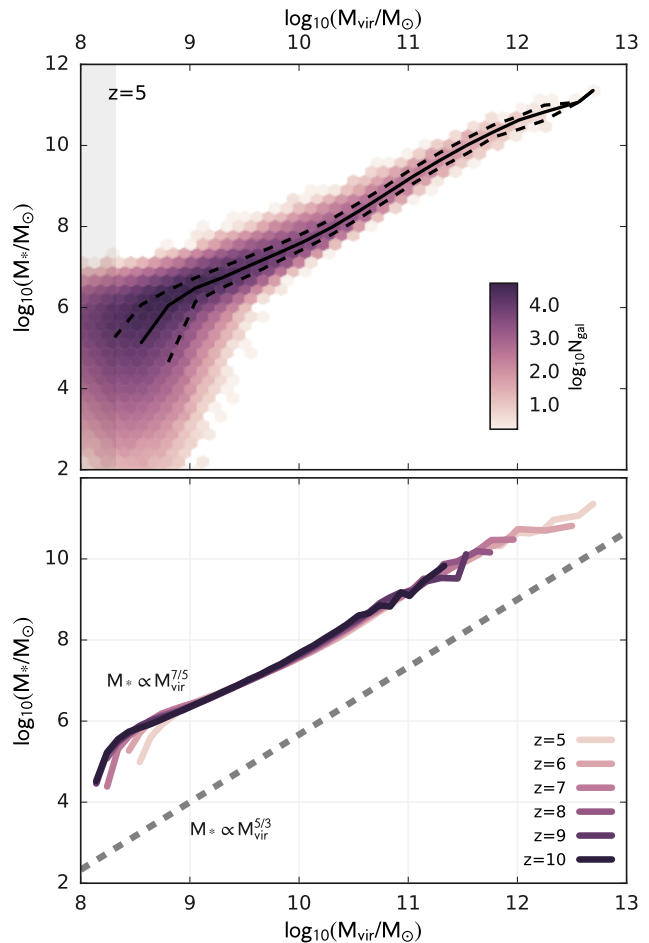


Figure 3. Upper: the distribution of total stellar mass as a function of FoF group virial mass for the *fiducial* model at $z=5$. The solid and dashed black lines show the median and 68% confidence intervals of the distribution. The grey shaded region indicates halo masses below the atomic cooling mass threshold. Lower: the evolution of the *fiducial* model median M_*-M_{vir} relation between redshifts 10–5. There is no significant evolution in either the slope or normalization with redshift. The grey dashed line indicates the theoretically motivated slope of $5/3$ (≈ 1.7) suggested by Wyithe & Loeb (2013) for supernova regulated galaxy growth. The normalization of this line has been arbitrarily chosen to allow a comparison with the slope of 1.4 predicted by MERAXES.

relation suggest that the normalization should evolve with redshift (Wyithe & Loeb 2003). Despite this, our model indicates that in order to reproduce the observed evolution of the galaxy stellar mass function over the redshifts considered in this work, the efficiency of galaxy formation and the associated feedback processes must conspire to provide a constant star formation efficiency in haloes of a fixed mass. This agrees with similar findings from subhalo abundance-matching (SHAM) studies at lower redshifts (e.g. Behroozi et al. 2013a).

In Fig. 4, we present the electron scattering optical depth of our fiducial model (blue line) against the current best observational measurements provided by the *Planck* satellite (Planck Collaboration 2015). The other model variations shown in this plot will be discussed in detail below.

⁴ Fits were carried out using flat priors in log space and a standard least-squares likelihood function. Poisson uncertainties were used for the model data points. All MCMC chains and posterior distributions were visually inspected for convergence.

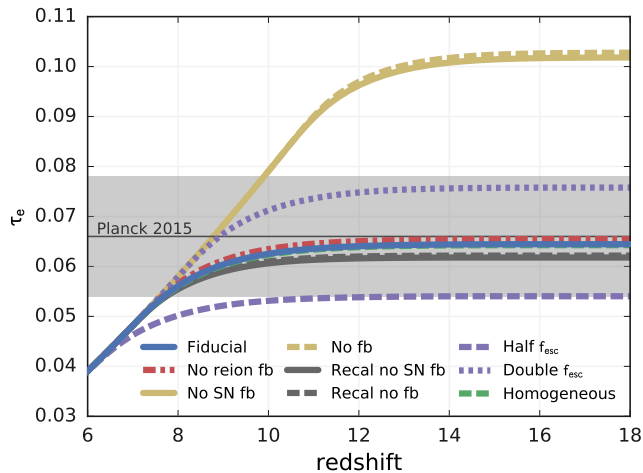


Figure 4. The integrated free electron scattering optical depth, τ_e , as a function of redshift. The grey horizontal line and shaded region indicate the constraints on τ_e to $z \sim 1100$ from the *Planck* 2015 data release (Planck Collaboration 2015). The blue solid line shows the fiducial model which is constrained to reproduce the *Planck* result. The *homogeneous* model result is obscured by the *fiducial* line.

However, as can be seen, our fiducial model provides an integrated optical depth which is in excellent agreement with the *Planck* results.

An important consideration when assessing the results of any cosmological simulation is the potential loss of stellar mass (and therefore ionizing photon contribution) due to finite mass resolution. This issue is explored in detail for MERAXES and the *Tiamat* suite of simulations in Appendix A. In summary, we find that the halo mass function of the full *Tiamat* simulation is complete down to approximately 0.5dex above the atomic cooling mass threshold at $z=5$, whilst the lower volume but higher mass resolution *Medi Tiamat* is fully complete down to this mass limit. Using *Medi Tiamat* to quantify the fraction of total stellar mass missing from the full simulation, we find that at $z=10$ we miss approximately 25% of stellar mass from low mass, unresolved systems. By $z=6$ this fraction falls to $\lesssim 5\%$.

Finally, in Fig. 5, we present a 4Mpc deep slab extracted from the *fiducial* MERAXES model (see Section 4 below) at a volume-averaged neutral fraction of 0.8 (left) and 0.3 (right). The orange regions indicate the neutral portions of the simulation volume, whilst the green structure shows the underlying matter distribution within the ionized bubbles. At early times, these ionized bubbles surround the peaks in the density field where the first galaxies form. As reionization progresses the bubbles begin to overlap, and by $x_{\text{HI}}=0.3$ a large ‘lane’ of ionized hydrogen, extending the entire length of the simulation volume is formed. The ability to investigate the distribution and evolution of bubble morphologies and the associated observable 21 cm power spectra is a key feature of our MERAXES framework and is investigated in detail in Paper V. In the middle and bottom rows of Fig. 5, we overplot the positions of a random 1/50th of the full galaxy population in the slab, selected at $x_{\text{HI}}=0.3$. The galaxies plotted in the $x_{\text{HI}}=0.8$ panels are the main progenitors of this subsampled population. In the middle row, the points are scaled by

the stellar mass of each galaxy, whilst in the bottom row they are scaled by their instantaneous star formation rates. The fact that fewer points are present in the star formation rate panels is a result of the bursty nature of star formation in the model meaning some fraction of galaxies have no ongoing star formation at any particular redshift.

4 THE INTERPLAY BETWEEN REIONIZATION AND GALAXY GROWTH

In this section, we use MERAXES to investigate the relative importance of reionization feedback for regulating both the growth of galaxy stellar mass and the timing and duration of the EoR. We also quantify how simple variations to the physics of reionization affect the galaxy stellar mass function, before finally elucidating the importance of local environment for determining the stellar mass of galaxies affected by photoionization suppression. We again note that the results of this work should be interpreted within the context of our chosen parameter values, constrained to match the evolution of the galaxy stellar mass function and the optical depth to electron scattering as described in Section 3.

Throughout we focus on the following model variations.

Fiducial (—): both the spatial and temporal evolution of the reionization structure and UVB intensity are fully coupled to the growth of the source galaxy population. This is the model calibrated in Section 3 above to match the evolution of stellar mass function and Thompson scattering optical depth measurements.

No feedback (—): the *fiducial* model with no supernova feedback or reionization feedback included, resulting in runaway star formation.

No supernova feedback (—): the *fiducial* model with supernova feedback turned off. All remaining physical processes, including reionization feedback, remain unchanged.

No reionization feedback (—): the *fiducial* model with reionization feedback removed by setting $f_{\text{mod}}=1$ for all galaxies at all times. All remaining physical processes, including supernova feedback, remain unchanged.

Recalibrated no supernova feedback (—): the *no supernova feedback* model with a lower star formation efficiency, $\alpha_{\text{SF}}=1.06 \times 10^{-3}$, chosen to replicate the total $z=5$ stellar mass density of the *fiducial* model.

Recalibrated no feedback (—): the *no feedback* model with the same lower star formation efficiency ($\alpha_{\text{SF}}=1.06 \times 10^{-3}$).

Half f_{esc} (—): the fully coupled *fiducial* model but with a lower escape fraction of $f_{\text{esc}}=0.1$.

Double f_{esc} (—): the fully coupled *fiducial* model but with a higher escape fraction of $f_{\text{esc}}=0.4$.

Homogeneous (—): the evolution of reionization is decoupled from that of the growth of galaxies. The baryon fraction modifier of each halo, f_{mod} , is determined using the halo number-weighted average M_{fit} as a function of redshift calculated using the *fiducial* model (see Section 2.11.2 above). All remaining physical processes remain unchanged from the *fiducial* case.

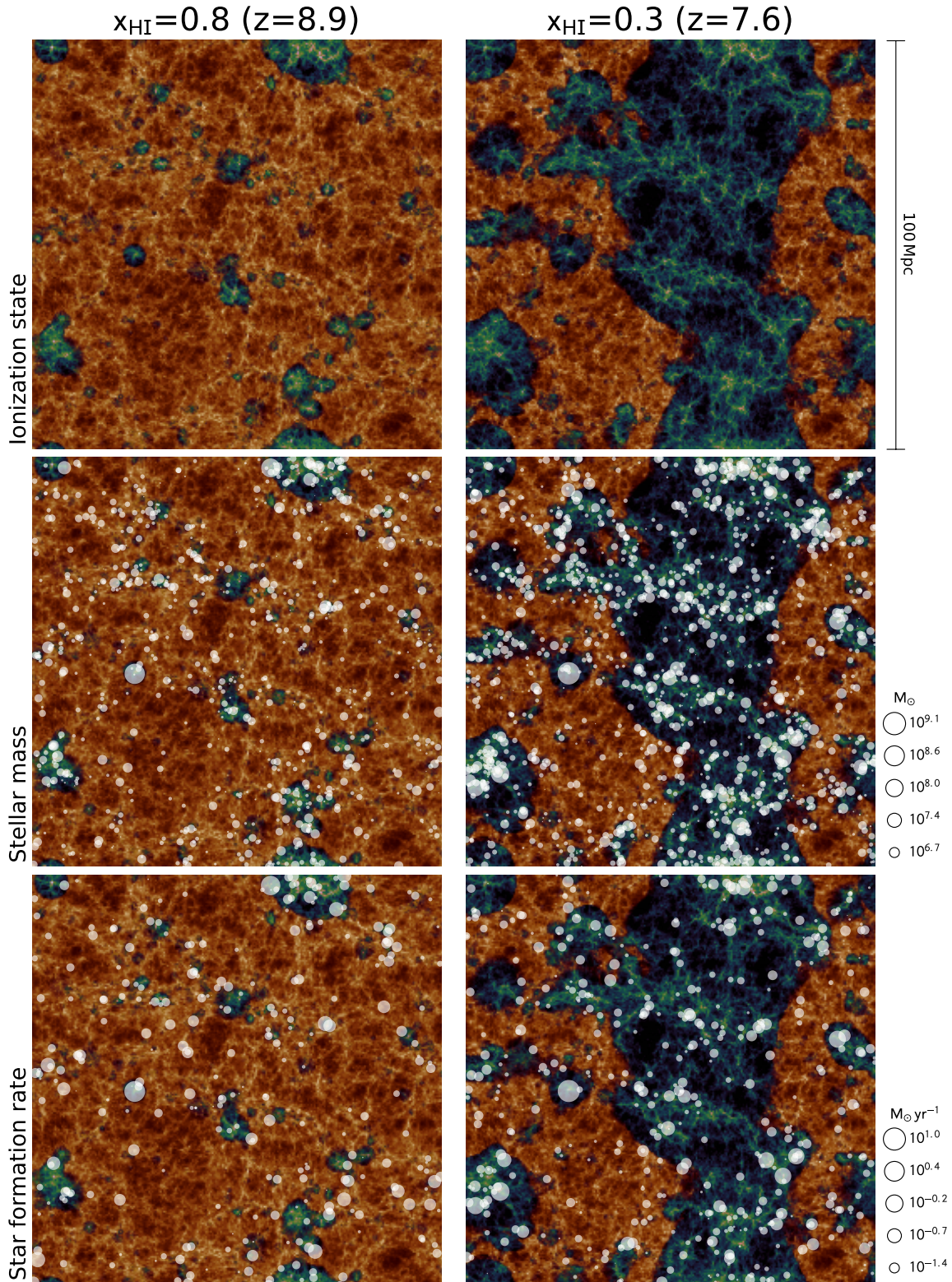











Figure 5. The ionization structure of a 4Mpc thick slab produced by MERAXES. The left- and right-hand columns correspond to a volume-weighted global neutral fraction of $\langle x_{\text{HI}} \rangle = 0.8$ and 0.3, respectively. Top row: the ionization state of the slab. Orange indicates regions of the volume which are neutral, whilst the green structure shows the underlying matter distribution inside the ionized bubbles surrounding the densest structures. At $\langle x_{\text{HI}} \rangle = 0.3$ (right), there is a large ‘lane’ of ionized IGM approximately 50Mpc wide extending from top to bottom where multiple bubbles overlap. Middle row: the same ionization structure with a random 1/50th of the ionizing galaxy population (selected at $\langle x_{\text{HI}} \rangle = 0.3$) overlaid as points scaled by stellar mass. Bottom row: the same galaxy population as above but with point size scaled by instantaneous star formation rate. There are fewer galaxies in this row, compared to above, due to the bursty nature of star formation resulting in some galaxies forming no new stars in the current snapshot.

Table 2. Summary table of the different model runs explored in this work (see Section 4). $\Delta z_{\text{rHI}}=0.8 \rightarrow 0.2$ indicates the redshift spanned between a global neutral fraction of 80% and 20%. The α_{SF} and f_{esc} columns indicate the star formation efficiency and ionizing photon escape fraction of each run respectively. The $z=5$, 6, and 7 SMF α parameters (last three columns) refer to the low mass slope of the corresponding stellar mass functions fit with a standard Schechter function. For reference, the α parameters measured by Duncan et al. (2014) are $-1.90^{+0.21}_{-0.16}$, $-1.91^{+0.91}_{-0.59}$ and $-2.31^{+1.31}_{-0.19}$ for redshifts 5, 6, and 7, respectively.

Model	α_{SF}	f_{esc}	$z_{\text{rHI}}=0.5$	$\Delta z_{\text{rHI}}=0.8 \rightarrow 0.2$	SMF α		
					$z=5$	$z=6$	$z=7$
 Fiducial	0.03	0.2	7.96	1.47	$-1.84^{+0.01}_{-0.01}$	$-1.92^{+0.02}_{-0.02}$	$-2.05^{+0.03}_{-0.03}$
 No reionization feedback	0.03	0.2	8.08	1.42	$-1.88^{+0.01}_{-0.01}$	$-1.96^{+0.02}_{-0.02}$	$-2.06^{+0.03}_{-0.03}$
 No SN feedback	0.03	0.2	11.41	1.52	$-1.69^{+0.01}_{-0.00}$	$-1.86^{+0.01}_{-0.01}$	$-2.04^{+0.01}_{-0.01}$
 No feedback	0.03	0.2	11.50	1.47	$-2.06^{+0.00}_{-0.00}$	$-2.14^{+0.01}_{-0.01}$	$-2.23^{+0.01}_{-0.01}$
 Recalibrated no SN feedback	0.00106	0.2	7.75	1.29	$-2.25^{+0.02}_{-0.02}$	$-2.51^{+0.03}_{-0.03}$	$-2.69^{+0.07}_{-0.06}$
 Recalibrated no feedback	0.00106	0.2	7.8	1.26	$-2.29^{+0.02}_{-0.02}$	$-2.52^{+0.03}_{-0.03}$	$-2.66^{+0.07}_{-0.07}$
 Half f_{esc}	0.03	0.1	6.89	1.38	$-1.85^{+0.01}_{-0.01}$	$-1.94^{+0.02}_{-0.02}$	$-2.05^{+0.03}_{-0.03}$
 Double f_{esc}	0.03	0.4	9.04	1.50	$-1.83^{+0.01}_{-0.01}$	$-1.91^{+0.02}_{-0.02}$	$-2.03^{+0.03}_{-0.03}$
 Homogeneous	0.03	0.2	7.94	1.50	$-1.84^{+0.01}_{-0.01}$	$-1.94^{+0.02}_{-0.02}$	$-2.06^{+0.03}_{-0.03}$

4.1 The relative importance of reionization feedback

In Section 3 above, we demonstrated that our *fiducial* model successfully reproduces the evolution of the high- z galaxy stellar mass function, as well as the most recent electron scattering optical depth measurements. In this section, we utilize the resulting realistic population of galaxies to investigate how important photoionization suppression of baryonic infall is for regulating the stellar mass content of dark matter haloes when compared to galactic feedback processes such as supernova feedback.

4.1.1 The stellar mass function

In Fig. 6 we show the $z=5$ (left) and $z=8$ (right) galaxy stellar mass functions from each of our model variations. The latter redshift value corresponds to a volume-averaged neutral hydrogen fraction of 50% in the *fiducial* model (—); cf. Fig. 9 and Table 2). The bottom panels also indicate the fractional differences of a subset of the models with respect to the fiducial result. Immediately apparent is that models without supernova feedback (—, —, —, —) produce the most significant change to the $z=5$ stellar mass function and are the only models which are not consistent with the observational data (grey points). The gold solid line (—) shows the predicted stellar mass content of haloes in the *no supernova feedback* model. Here, reionization feedback is still included using the fiducial escape fraction of $f_{\text{esc}}=0.2$; however, it is unable to counter the runaway star formation which occurs in the absence of supernova feedback. The net result is a large boost in the number densities of galaxies with respect to the *fiducial* model (—) for $M_* \lesssim 10^{10.5} M_{\odot}$. At higher masses, supernova feedback becomes inefficient and the mass function converges to the *fiducial* result. This is because these large galaxies preferentially reside in the most massive haloes where supernovae are unable to provide the required energy to heat gas to/beyond the virial temperature, thus preventing it from being used for further star formation (cf. Section 2.5 and equations therein).

The red dash-dotted line (—) in Fig. 6 shows the results of our *no reionization feedback* model. Here we use the fiducial escape fraction of $f_{\text{esc}}=0.2$ in order to calculate the

ionization state of the IGM; however, we decouple the effect of photoionization suppression from the infall of baryons into each FoF group by setting $f_{\text{mod}}=1$ (cf. Equation 1) for all groups at all times. Hence, in this model variation, galaxy evolution proceeds independently of the ionization state of the IGM. By turning off reionization feedback in this manner whilst still leaving the strong supernova feedback required to reproduce the observed high- z stellar mass functions in place, we find little change to the stellar mass function during the EoR (right panel) with respect to the *fiducial* model (—). However, the effects of reionization are cumulative over time (see Equation 32) and by $z=5$ (left panel) we find the space density of galaxies with stellar masses less than $10^7 M_{\odot}$ is increased by up to $\sim 40\%$ relative to the *fiducial* result. However, this effect is small compared to that found in the absence of supernova feedback. Furthermore, as we move to higher masses, the relative differences rapidly decrease. This is a reflection of the fact that reionization feedback is only effective in low-mass haloes (hosting typically low-mass galaxies) with shallow potential wells susceptible to accretion suppression from the UVB (cf. Section 4.1).

By comparing the *no feedback* (—) and *no supernova feedback* (—) model lines, we can investigate the isolated impact of reionization on the growth of galaxy stellar mass. In the former model, there is no reionization or supernova feedback included; however, in the latter we turn on the photoionization suppression of baryon accretion. This results in a clear decrement in the number density of low mass galaxies with $M_* \lesssim 10^9 M_{\odot}$ at $z=5$. Higher mass galaxies are largely unaffected since, by the time their massive host haloes were exposed to the UVB, they already provided a potential well deep enough to accrete gas despite the presence of the photoionizing UVB. During reionization (right-hand panel), we see that the effects of reionization feedback are more modest due to a smaller fraction of galaxies being exposed to the UVB as well as the typically shorter exposure times for those which have.

Simply turning off supernova feedback whilst leaving the remaining model parameters constant (*no supernova feedback*; —) leads to an over-prediction of the total $z=5$ stellar mass density by a factor of 5 relative to the *fiducial* model as well as a mass function slope which is too steep

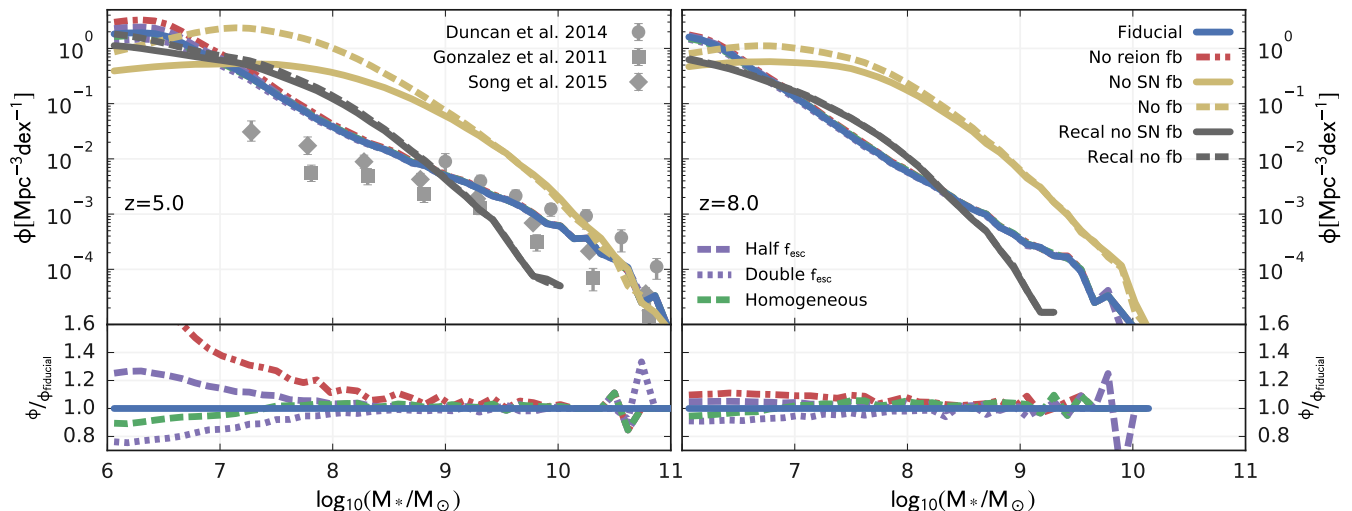


Figure 6. The $z=5$ and 8 galaxy stellar mass functions. The solid blue line indicates the result of the *fiducial* patchy reionization model which has been calibrated to reproduce the observed $z=5-7$ mass functions. Grey points in the left-hand panel show the relevant observational data. The small difference introduced by omitting reionization feedback (red dash-dotted) demonstrates the minor role which this mechanism plays in regulating stellar mass growth. Conversely, the removal of supernova feedback (gold solid) produces a much larger effect. However, comparison between the *no feedback* (gold dashed) and *no supernova feedback* (grey solid) models shows that, in the absence of the dominant supernova feedback, reionization does suppress the number density of $M_* \lesssim 10^9 M_\odot$ galaxies if star formation is gas supply limited in a large fraction of haloes.

to be consistent with observations. This enhanced star formation may lead to an under-estimate in the importance of reionization feedback. In order to test this hypothesis we have run a *recalibrated no supernova feedback* model (—) with a reduced star formation efficiency parameter, α_{SF} , chosen to provide the same total $z=5$ stellar mass density as the *fiducial* model. The *recalibrated no feedback* model (—) additionally shows the result of this altered α_{SF} with reionization feedback also omitted. Again, these models predict a stellar mass function which is too steep to be consistent with observations. However, we find that there is no combination of remaining parameters in our model which can reproduce the slope of the observed stellar mass function in the absence of supernova feedback.

The small relative difference between the *recalibrated no supernova feedback* and *recalibrated no feedback* models in Fig. 6 indicates that reionization feedback is even less effective at regulating galaxy growth than was the case with the original *no supernova feedback* and *no feedback* variations. This is because our fiducial star formation efficiency parameter results in stellar mass growth in the majority of small haloes being gas supply limited. By reducing the star formation efficiency parameter in the recalibrated models, this is no longer the case and there is more gas available in these systems than can be converted into stars in a single time step. Reionization-driven photosuppression of accretion into these gas-rich systems therefore has little impact on the growth of stellar mass, resulting in a quantitatively similar change to the stellar mass function as is found in the presence of supernova feedback (i.e. comparing the *fiducial* and *no reionization feedback* model results).

Together, these results highlight an over-estimate of the importance of reionization feedback for regulating star formation in models which do not employ the galactic feedback processes necessary to reproduce the observed stellar mass

functions at high- z . Alternatively, at the very least, a star formation efficiency low enough to result in a gas-rich star formation scenario is needed.

4.1.2 The stellar mass content of haloes

In Section 4.1.1, we demonstrated that the impact of reionization on regulating the growth of galaxies and the production of ionizing photons in MERAXES is minimal owing to the importance of supernova feedback. In this section, we explore this topic further by investigating the stellar mass content of haloes as predicted by a subset of our model variations, both subsequent to and during reionization. In Fig. 7, we present the fraction of baryons in the form of stars, $f_* = M_*/(f_b M_{\text{vir}})$, as a function of FoF group virial mass, at $z=5$ and 8 (the latter redshift corresponding to $x_{\text{HI}} \sim 0.5$ in the fiducial model). Thick lines indicate the results from running MERAXES on the full *Tiamat* simulation. Thin lines show a subset of the same models run on the higher resolution *Medi Tiamat* trees which are complete down to the atomic cooling mass threshold at both redshifts shown (cf. Appendix A).

At low halo masses, there are minor differences between the *fiducial* model results of each simulation. These are predominantly driven by an increased prevalence of merger-driven halo mass growth in *Medi Tiamat* which is unresolved in the lower resolution *Tiamat* trees. These merger events occur less frequently than *in situ* star formation episodes, but they are more efficient, giving rise to more energetic supernova feedback episodes capable of ejecting significant amounts of material from haloes and temporarily halting star formation. The net result is a reduction in the stellar mass growth of low mass haloes in the higher resolution trees. During reionization (right-hand panel), the lower atomic cooling mass threshold results in *Tiamat* missing a

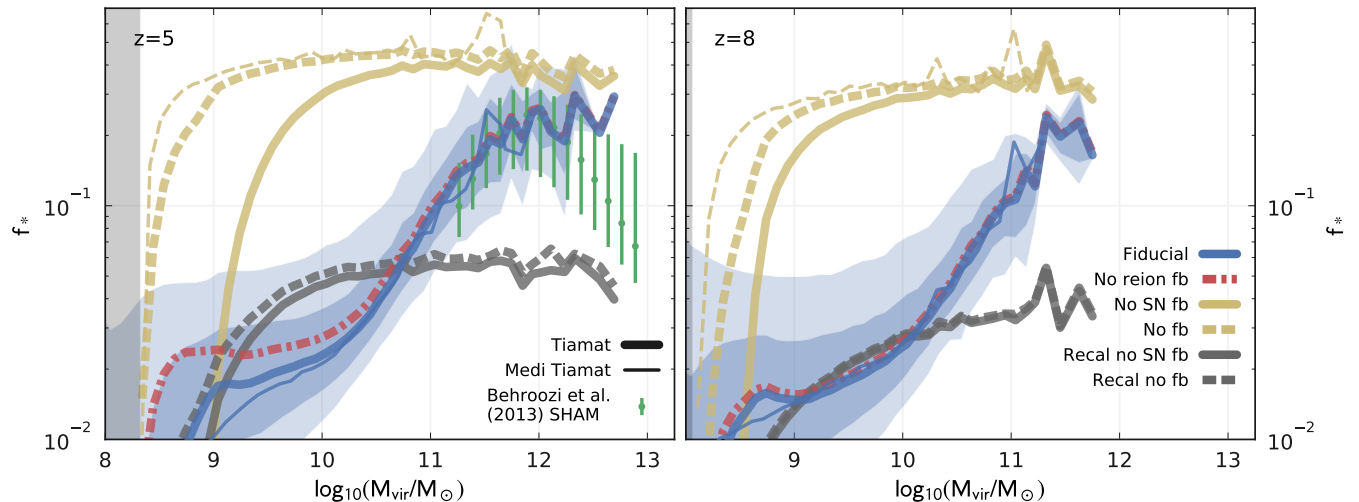


Figure 7. The median fraction of baryons in the form of stars, $f_* = M_*/(f_b M_{\text{vir}})$, as a function of FoF group mass, at $z=5$ (left) and $z=7.8$ (right). Thick lines show the results of MERAXES when run on the full *Tiamat* simulation merger trees, whilst thin lines indicate the results of running on the higher resolution *Medi Tiamat* trees. The blue solid lines and surrounding shaded regions show the median result of the *fiducial* (*Tiamat*) model and associated 68 and 95% confidence intervals. The magnitudes of these statistical uncertainties are representative of those of all of the models shown in each panel. The grey shaded region at the left of each panel denotes halo masses below the atomic cooling mass threshold, $M_{\text{cool}}(z)$, corresponding to a virial temperature of 10^4 K. The green data points in the $z=5$ panel display the SHAM results of Behroozi et al. (2013b) which are in excellent agreement with our *fiducial* model. Comparison between the *no feedback* (gold dashed) and *no supernova feedback* (grey solid) lines demonstrates that reionization feedback is most effective in low mass haloes. However, supernova feedback of the level required to reproduce the observed high- z stellar mass functions dominates the suppression of star formation across all halo masses. The strong halo mass dependence of f_* contrasts the constant value assumed by the majority of reionization structure studies.

larger fraction of the lowest mass haloes than is the case at $z=5$. This can be seen by comparing the *no feedback* (—) model lines from each simulation. However, when feedback is included, the stellar mass content of these haloes is greatly reduced and the results of the different simulations again come to a good agreement. We also note that despite the minor discrepancies at low masses, there is excellent overall agreement between the *Tiamat* and *Medi Tiamat* results across all other masses in both panels. Hence, Fig. 7 demonstrates that our full *Tiamat* volume has sufficient mass resolution to correctly model the growth of galaxies across the range of masses and redshifts relevant for this work.

Our *fiducial* model (—) predicts a strong decline in the stellar mass content of haloes with $M_{\text{vir}} \lesssim 10^{12} M_{\odot}$. For comparison, a constant stellar baryon fraction of $f_* \sim 0.05$ is commonly employed by previous studies utilizing 21CM-FAST (e.g. Mesinger et al. 2011; Sobacchi & Mesinger 2013), as well as previous N -body-based radiative transfer calculations (e.g. Iliev et al. 2007). Whilst it is important to remember that, for the purposes of reionization, the precise value of f_* is degenerate with other quantities such as the escape fraction of ionizing photons, it is clear that the approximation of a constant value with halo mass is poor. Correctly predicting and self-consistently utilizing this relation is a key feature of MERAXES, as is investigating and predicting further potential contributing variables such as environmental density (see Section 4.5 below) and ionizing escape fraction.

For comparison, we have also plotted the $z=5$ f_*-M_{vir} relation and $1-\sigma$ scatter found by the SHAM study of Behroozi et al. (2013b, green error bars). Our *fiducial* model (—)

shows excellent agreement with these results.⁵ This is perhaps not unexpected given that both studies have utilized N -body simulations with free model parameters constrained to match observed high- z stellar mass functions. However, the agreement is still noteworthy given that we have utilized different N -body simulations, halo finders, observational data sets and methodologies. Less obvious is the high level of agreement between the scatter in f_* values at a fixed M_{vir} which is an unconstrained prediction of our MERAXES results. We also highlight that our model provides predictions down to masses at least two orders of magnitude lower than can be directly probed by current observations and SHAM studies.

A notable feature of the *no feedback* model (—) is the sharp turn-over in the f_*-M_{vir} relation at halo masses approaching, but greater than, the atomic cooling mass threshold. This occurs in both the full *Tiamat* (thick lines) and higher resolution *Medi Tiamat* volumes (thin lines), indicating that this is a robust prediction of our model. Further investigation suggests that stellar mass growth in these low mass haloes is almost entirely dominated by *in situ* star formation (as opposed to merger driven growth). However,

⁵ We note that the SHAM results of Behroozi et al. (2013b) actually provide the f_*-M_{vir} relation for central subhaloes, not for FoF groups as we have presented in Fig. 7. However, at the high halo masses probed by the abundance matching data, the central subhalo and its galaxy dominate the mass of the FoF group in the vast majority of cases. Therefore this comparison is fair. We have also explicitly confirmed that the subhalo f_*-M_{vir} relation of our *fiducial* model, as well as its scatter, remain consistent with the above results over the relevant mass range.

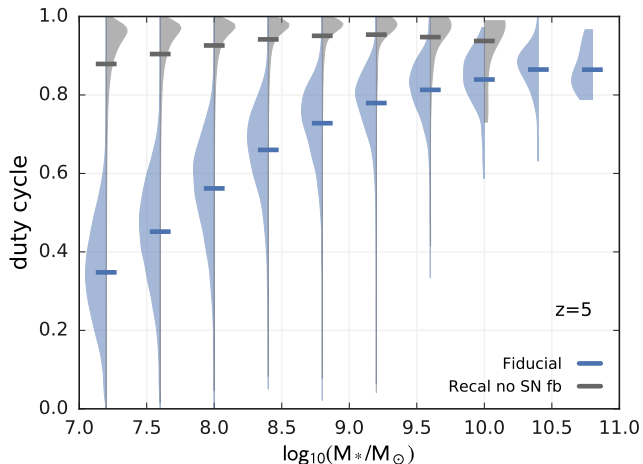


Figure 8. The fraction of time over which galaxies have been actively forming stars during their lifetimes (duty cycle) as a function of their $z=5$ stellar mass in both the *fiducial* (blue) and *recalibrated no supernova feedback* (grey) models. The shaded regions show a kernel-density estimate of the distribution of duty cycles for each stellar mass bin whilst horizontal bars indicate the mean values. Supernova feedback in the *fiducial* model blows out cold gas in low mass systems, stifling star formation and reducing the fraction of time over which they are actively forming stars. In the *recalibrated no supernova feedback* model, the lack of supernova feedback coupled with a low star formation efficiency results in the ample availability of cold gas at all times and hence a duty cycle of ~ 1 at all masses.

the fraction of their lifetimes over which the galaxies hosted by these objects have been actively forming stars is small. This is due to an inability to obtain enough gas to exceed the critical surface density required for star formation (cf. Equation 5).

By comparing the *no feedback* (■) and *no supernova feedback* (■) model lines we can again assess the importance of reionization-driven photosuppression in the absence of the effects of supernova feedback. In these models, the star formation efficiency in a significant number of low-mass haloes remains gas supply limited and hence reducing the infall of fresh baryons via photoionization suppression has a significant effect. Comparing the *recalibrated no feedback* (■) and *recalibrated no supernova feedback* (■) model lines, where the lowered star formation efficiency results in galaxy growth which is no longer limited by the availability of cold gas, the effect of reionization is far less pronounced, just as is the case in the model variations with supernova feedback included (i.e. the *fiducial* and *no reionization feedback* models).

To demonstrate the effect of gas supply limited star formation more explicitly, in Fig. 8 we present the fraction of their lifetime over which galaxies have been actively forming stars (i.e. their duty cycle) as a function of stellar mass in both the *fiducial* (blue) and *recalibrated no supernova feedback* (grey) models. The shaded regions show a kernel-density estimate of the distribution of duty cycles for each stellar mass bin whilst horizontal bars indicate the mean values. In the *fiducial* model, supernova feedback reduces the availability of cold gas for star formation, such that only a small fraction of the infalling material is converted to stars

in low mass systems. In the *recalibrated no supernova feedback* model, the lack of supernova feedback, coupled with a low star formation efficiency, means that there is an ample supply of cold gas for star formation at all times and hence a duty cycle of ~ 1 at all masses.

4.2 Quantifying the effects of reionization on the galaxy stellar mass function

Having demonstrated the relatively small importance of reionization feedback for regulating galaxy growth, in this section we move on to quantify the effects of varying the escape fraction of ionizing photons on the stellar mass function. The ability to self-consistently and quantitatively investigate such outcomes is a key feature of MERAXES.

In Fig. 6 we present the stellar mass functions predicted by our *double f_{esc}* (■) and *half f_{esc}* (■) models. By doubling the escape fraction of ionizing photons, we see a suppression in the stellar mass function by around 20% for masses of around $10^7 M_{\odot}$. The reason is that by increasing the ionizing emissivity of all galaxies, reionization occurs earlier than in the *fiducial* model (see Fig. 9). This results in an increased time over which haloes are exposed to ionizing radiation. Coupled with the fact that haloes are typically less massive and more susceptible to the effects of reionization at higher redshifts, the final result is a suppression in the number of low mass galaxies relative to the *fiducial* model. The space density of more massive objects is again largely unaffected since, even with an earlier exposure to the ionizing UVB, their haloes were already massive enough to accrete gas from the reionized IGM. Any reduction in the stellar mass of these objects is hence mainly driven by the accretion of less stellar mass through mergers. By halving the escape fraction of ionizing photons (*half f_{esc}* model; ■), we obtain a mirror effect. Reionization occurs later, and hence haloes are typically exposed to the UVB for less time and have larger masses when this occurs.

Current observations are only able to probe the $z=5$ stellar mass function down to $M_{*} \gtrsim 10^{7.5} M_{\odot}$, and even then only through the use of uncertain mass-to-light ratios (e.g. González et al. 2011; Song et al. 2016) with relatively large systematic and statistical uncertainties. Thus, even in the case of no reionization feedback, the relative change between the mass functions of Fig. 6 is well below the level of observational uncertainties. In Table 2, we indicate the low-mass slope, α , for each run, where we have only fitted to galaxies with stellar masses greater than the observational limit of $10^{7.5} M_{\odot}$. The differences between the resulting α values are again too small to be detected observationally without extremely precise measurements beyond what is currently achievable. On the right-hand side of Fig. 6, we present the equivalent galaxy stellar mass functions at $z=8$, corresponding to a global neutral hydrogen fraction of approximately 0.5 in the *fiducial* model (Table 2). Here, even at the resolved masses, the variations in space density with respect to the *fiducial* model are typically less than 10%. This suggests that the statistics of low redshift ($z \leq 5$) galaxy populations, as opposed to galaxies during the EoR itself, provide the stronger potential constraints on reionization.

On the other hand, the insensitivity of the observable portion of the $z=5$ mass function to the details of reionization suggests that we can calibrate our galaxy formation models

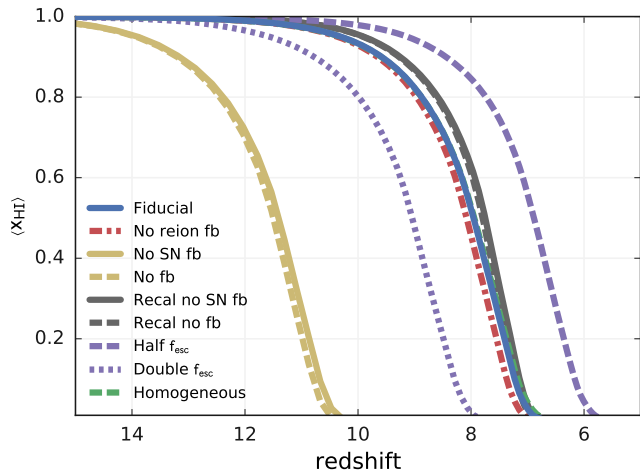


Figure 9. The evolution of the volume-weighted global neutral fraction, $\langle x_{\text{HI}} \rangle$, as a function of redshift. The blue solid line indicates the result of our *fiducial* model which matches both the observed evolution of the galaxy stellar mass function (Fig. 2) and the most recent electron scattering optical depth measurements (Fig. 4). The small perturbation to the neutral fraction history caused by the omission of reionization feedback (red dash-dotted) indicates that the EoR is not self-regulated. Instead, supernova feedback is almost entirely responsible for regulating the production of ionizing photons and the progression of reionization. The *homogeneous* and *recalibrated no feedback* lines are obscured by the *fiducial* and *recalibrated no supernova feedback* results, respectively.

to high-redshift stellar mass/luminosity functions and then use additional observations to constrain other unknowns in high- z galaxy formation. These include the dependence of the ionizing escape fraction on properties such as mass, redshift and star formation rate.

4.3 The evolution of ionized hydrogen in the IGM

In Fig. 9, we present the evolution of the volume-averaged neutral fraction of our *fiducial* patchy reionization model (—) and all eight model variations. The second and third columns of Table 2 also provide some basic statistics on the timing and duration of reionization in each model in the form of the redshift at which the volume becomes 50% ionized ($z_{x_{\text{HI}}=0.5}$) and the redshift spanned between neutral fractions of 80 and 20% ($z_{x_{\text{HI}}=0.8 \rightarrow 0.2}$).

The purple lines in Fig. 9 demonstrate the effect of either doubling (••••) or halving (—) the ionizing escape fraction from its fiducial value of $f_{\text{esc}}=0.2$. This shifts reionization to earlier and later times, respectively, but produces no significant change to its duration (Table 2). Interestingly, Fig. 4 shows that, despite a relative shift in the midpoint of reionization with respect to the *fiducial* model of $\Delta z \approx \pm 1$, both the double and half ionizing escape fraction models provide reionization histories which are marginally consistent with the *Planck* optical depth constraints. Furthermore, the relative change in τ_e with respect to the *fiducial* model is approximately symmetric (Table 2). As demonstrated in Section 4.2, the effect of reionization feedback on the growth of stellar mass is weak, with both of these model varia-

tions predicting stellar mass functions which remain in good agreement with observational data. Hence, f_{esc} is effectively decoupled from the stellar mass function in our model and the electron scattering optical depth measurements can be directly translated to an approximate constraint on this parameter.⁶ In the case of an ionizing escape fraction which is constant with both mass and redshift, $0.1 \lesssim f_{\text{esc}} \lesssim 0.4$ for our fiducial model.

Changing the escape fraction of ionizing photons has two competing outcomes for reionization. First, the ionizing efficiency parameter, ξ , is directly proportional to f_{esc} (cf. Equation 30), and so doubling the escape fraction results in a doubling in the efficiency of reionization for a fixed mass of stars. As a consequence, the first galaxies to form have a larger impact, moving the start of reionization to earlier times. To balance this, the increased ionizing emissivity also leads to a more efficient photoionization suppression of baryonic infall, reducing star formation rates and regulating the production of further ionizing photons. The converse is also true for the case of halving the escape fraction. Here, more stellar mass is required to produce the same number of ionizing photons escaping into the IGM; hence, reionization moves to later times. To counter this, the UVB photosuppression of baryonic infall is also reduced. This ‘self-regulation’ mechanism has been proposed as a potentially important effect for modulating the timing and duration of reionization (Iliev et al. 2007).

We can exploit our framework to quantify just how effective photoionization suppression is in self-regulating reionization for a realistic population of galaxies which simultaneously reproduces both the growth of stellar mass in the early Universe and current optical depth constraints. In Fig. 9 we again show the results of our *no reionization feedback* model (—••) in which galaxy evolution proceeds independently of the ionization state of the IGM. As can be seen in Fig. 9, the resulting change to the evolution of the global neutral fraction with respect to the *fiducial* model is minimal, with a shift in the midpoint of reionization of less than 0.1 in redshift (cf. Table 2). This is easily understood by considering the minor role which reionization suppression plays in modulating star formation, and hence the production of ionizing photons, during the EoR itself (cf. Section 4.1 above). Our MERAXES framework thus predicts that reionization is not self-regulated, supporting similar claims made by other authors (e.g. Kim et al. 2013b; Sobacchi & Mesinger 2013; Wyithe & Loeb 2013).

Instead, the strong importance of galactic feedback processes (such as supernova feedback) for regulating the growth of stellar mass leads to them being dominant in controlling the timing and duration of reionization along with f_{esc} . The gold solid line (—) in Fig. 9 shows the predicted neutral fraction evolution in the absence of supernova feedback processes (*no supernova feedback* model). The resulting runaway star formation, in tandem with the fiducial escape fraction of $f_{\text{esc}}=0.2$, results in an early and rapid reionization process with a midpoint at $z=11.2$ and a time of just

⁶ We emphasize that the ability of the electron scattering depth to fully constrain f_{esc} is only true within the framework of our model where other confounding processes, such as the intrinsic ionizing photon production rate of stellar populations, are fixed.

71 Myr between volume averaged neutral fractions of 80 and 20%. We also show in Fig. 9 the *no feedback* model, where neither reionization nor supernova feedback is included. The small perturbation to the reionization history with respect to the *no supernova feedback* model (where only reionization feedback is included) is again extremely small (see also Table 2). The same is also true of the *recalibrated no feedback* (—■) and *recalibrated no supernova feedback* (—●) models, further reinforcing the negligible contribution of photosuppression in self-regulating reionization.

In summary, the level of supernova feedback required to reproduce observed high- z stellar mass functions dominates over photoionization suppression with regard to modulating the progression of reionization. This agrees with the results of previous works (e.g. Kim et al. 2013b; Wyithe & Loeb 2013). However, we do note that if reionization were more extended than is predicted by our models, the role of reionization feedback may be enhanced. For example, inhomogeneous IGM recombinations or a redshift-varying escape fraction of ionizing photons (see Section 4.4 below) could delay the end stages of reionization and lead to an enhanced suppression of the large-scale reionization structure (Sobacchi & Mesinger 2014).

Finally, for reference, the green dashed line (—■) of Fig. 9 shows the neutral fraction evolution of the *homogeneous* model variation. This model produces a reionization history which is in excellent agreement with the fiducial self-consistent, spatially dependent scenario (—●) by construction. This is due to the fact that the *homogeneous* model was calibrated to reproduce the same mean filtering mass as the *fiducial* model at all redshifts. However, we will go on to show in Section 4.5 that the use of a parametrized homogeneous model such as this has important, environmentally dependent implications for the predicted properties of individual galaxies.

4.4 The evolution of the instantaneous ionizing emissivity

Having demonstrated that reionization feedback plays only a minor role in regulating the evolution of the global neutral fraction, we now focus on elucidating the dominant effects of supernova feedback. In Fig. 10, we present the probability distribution function of instantaneous ionizing photon contributions as a function of FoF group virial mass for both the *fiducial* and *recalibrated no supernova feedback* models at various neutral fractions. At high x_{HI} (high- z), massive haloes have not had time to form and so the ionizing emissivity is dominated by masses near the atomic cooling mass threshold in both models. After reionization has begun, the distributions predicted by the two models rapidly begin to diverge, with our *fiducial* model predicting a broad range of contributing halo masses. This is due to the inclusion of supernova feedback which suppresses the relative ionizing photon contribution of low-mass systems. In the *recalibrated no supernova feedback* model variation, the absence of supernova feedback means that low-mass haloes instead remain the dominant source of ionizing photons at all times.

In Fig. 11, we show the evolution of the instantaneous ionizing emissivity, \dot{N}_{ion} , in units of ionizing photons per hy-

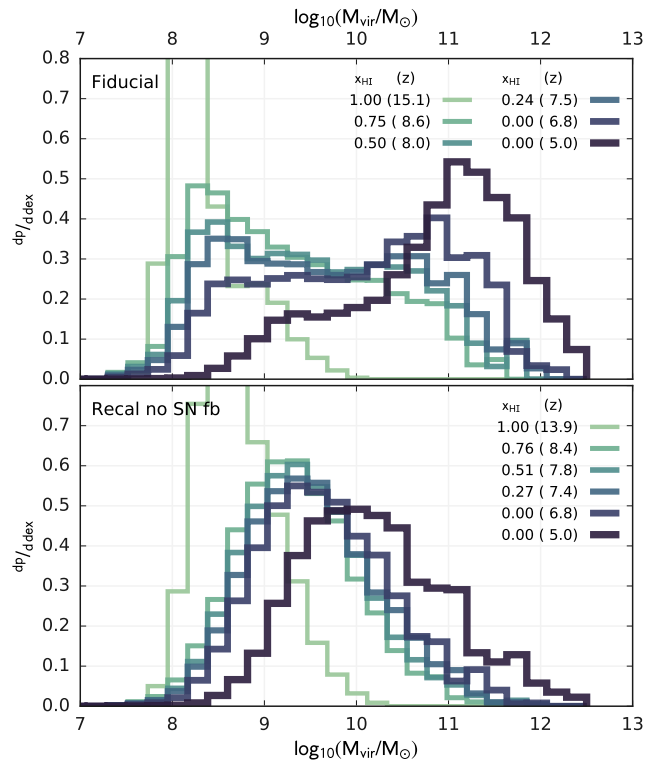


Figure 10. The probability distributions of instantaneous ionizing photon contribution as a function of FoF group mass for various global neutral fractions in the *fiducial* (top) and *recalibrated no supernova feedback* (bottom) models. The inclusion of supernova feedback in the *fiducial* model results in a broad distribution of halo masses which contribute to reionization.

drogen atom per Gyr:

$$\dot{N}_{\text{ion}} = \frac{\Delta m_*}{\Delta t} \frac{N_\gamma f_{\text{esc}}}{f_b M_{\text{tot}} (1 - 0.75 Y_{\text{He}})} = \frac{\Delta m_*}{\Delta t} \frac{\xi}{M_{\text{tot}}}, \quad (38)$$

where ξ is the ionizing efficiency as defined in Equation 30 and Δm_* is the change in gross stellar mass (excluding losses due to stellar evolution) between two consecutive snapshots separated by a time Δt . The data points present recent measurements derived by combining observed IGM Lyman α opacities with detailed hydrodynamical simulations including radiative transfer (Bolton & Haehnelt 2007; McQuinn et al. 2011; Becker & Bolton 2013).

Despite correctly reproducing the electron scattering optical depth (see Section 3), our *fiducial* model (—●) predicts a high and steeply increasing ionizing emissivity at $z=5$ that is inconsistent with the observational data. By construction, the *recalibrated no supernova feedback* model (—●) predicts a $z=5$ global emissivity in agreement with the *fiducial* result. However, the absence of supernova feedback leads to a steeper evolution with redshift in the recalibrated model. This is due to the lower star formation efficiency causing a delay in the build-up of significant stellar mass, and therefore the onset of reionization. As shown in Fig. 10, as galaxies grow with decreasing redshift, the absence of supernova feedback ensures that low-mass, low-bias haloes continue to dominate ionizing photon production. This leads to a more rapid growth in the global emissivity and a faster reionization process for $\langle x_{\text{HI}} \rangle \lesssim 0.5$ (cf. Fig. 9).

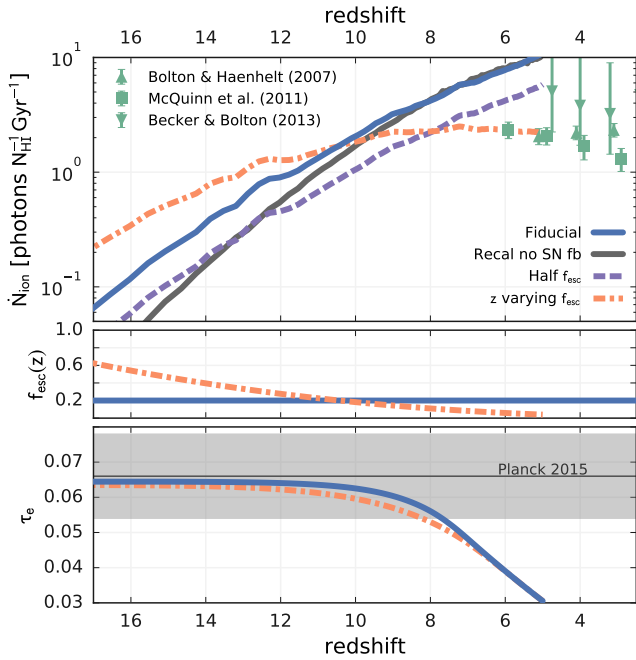


Figure 11. Top panel: the evolution of the ionizing emissivity in units of photons per hydrogen atom per Gyr. The green data points are taken from works combining IGM Lyman α opacities with detailed hydrodynamical simulations (Bolton & Haehnelt 2007; McQuinn et al. 2011; Becker & Bolton 2013). Both the *fiducial* (solid blue) and *recalibrated no supernova feedback* (solid grey) models overpredict the instantaneous ionizing efficiencies by a factor of ~ 5 at $z=5$. The *half f_{esc}* model (purple dashed), which is only marginally consistent with the *Planck* optical depth measurements, still fails to reproduce the observational data. However, an evolving escape fraction (orange dash-dotted) can simultaneously reproduce the observed flat emissivity and its normalization at $z \leq 6$. Middle panel: the escape fraction as a function of redshift for the *z -varying f_{esc}* model shown in the panel above. Bottom panel: the integrated free electron scattering optical depth, τ_e , as a function of redshift for the *fiducial* and *z -varying f_{esc}* models. The grey horizontal line and shaded region indicate the constraints on τ_e to $z \sim 1100$ from the *Planck* 2015 data release (Planck Collaboration 2015).

One possible modification to reduce the ionizing emissivity of the *fiducial* model, and thus bring it into qualitative agreement with the observational constraints from the Lyman α forest, would be to reduce the escape fraction of ionizing photons. As shown in Fig. 4, the *half f_{esc}* model (—) provides the lowest escape fraction that is consistent with the *Planck* optical depth constraints. However, from Fig. 11 we see that this model still results in a steep emissivity evolution which fails to reproduce the trend of the $z \leq 6$ Lyman α forest constraints. We can easily understand this result by noting that $\dot{N}_{\text{ion}} \propto f_{\text{esc}}$ (Equation 38). Therefore, halving f_{esc} simply results in a halving of \dot{N}_{ion} .

4.4.1 An evolving escape fraction

We now investigate how we can modify our model in order to simultaneously match the normalization and flat slope of the observed ionizing emissivity at $z \leq 6$, as well as our fiducial constraints of the *Planck* τ_e measurements and high- z galaxy

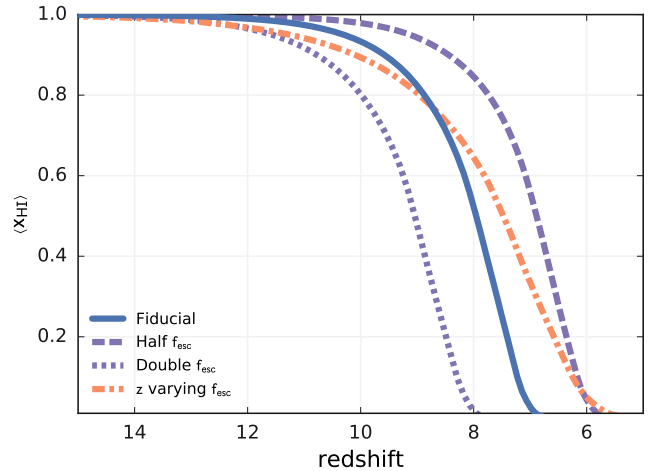


Figure 12. The evolution of the volume-weighted global neutral fraction, $\langle x_{\text{HI}} \rangle$, as a function of redshift for the *z -varying f_{esc}* model (orange dashed). Also shown for comparison are the results of the *fiducial* (blue solid), *half f_{esc}* (purple dashed), and *double f_{esc}* (purple dotted) models. The high escape fraction at high redshift in the *z -varying f_{esc}* model leads to the early onset of reionization, whilst the declining f_{esc} with decreasing redshift also prolongs its duration.

stellar mass functions. To fully address this question would require a full statistical investigation of the model’s free parameter space, a task which is beyond the scope of this work. However, the value of f_{esc} for an individual galaxy is strongly dependent on its chemical, structural, and kinematic properties, and there exists considerable theoretical and observational evidence to suggest that the average f_{esc} does indeed vary with redshift, mass, and/or star formation rate (e.g. Gnedin et al. 2008; Wise & Cen 2009; Paardekooper et al. 2011; Yajima et al. 2011; Kuhlen & Faucher-Giguère 2012; Mitra et al. 2013; Paardekooper et al. 2015).

In Fig. 11, we show the results of a *z -varying f_{esc}* model (—) which utilizes a modified version of the single power-law relation proposed by Kuhlen & Faucher-Giguère (2012):

$$f_{\text{esc}}(z) = \min \left[f_{\text{esc}|z=5} \left(\frac{1+z}{6} \right)^{\kappa}, 1 \right]. \quad (39)$$

The free parameters of this relation, $f_{\text{esc}|z=5}=0.04$ and $\kappa=2.5$, have been chosen to reproduce the McQuinn et al. (2011) ionizing emissivity and *Planck* τ_e measurements. We note that these values agree well with the range of values found by Kuhlen & Faucher-Giguère (2012) to simultaneously reproduce the observed UV luminosity function⁷, ionizing emissivity, and electron scattering optical depth. The middle panel of Fig. 11 shows the corresponding evolution of $f_{\text{esc}}(z)$.

In order to self-consistently implement a varying escape fraction in our model, we remove f_{esc} from the H II ionizing emissivity and efficiency equations (Equation 30 and 35 respectively) and instead track the build-up of the $f_{\text{esc}}(z)$ -weighted gross stellar mass of each galaxy. This weighted

⁷ Assuming a low luminosity cut-off of $M_{\text{UV}} \lesssim -14$, equivalent to the resolution limit of our simulation (Paper IV).

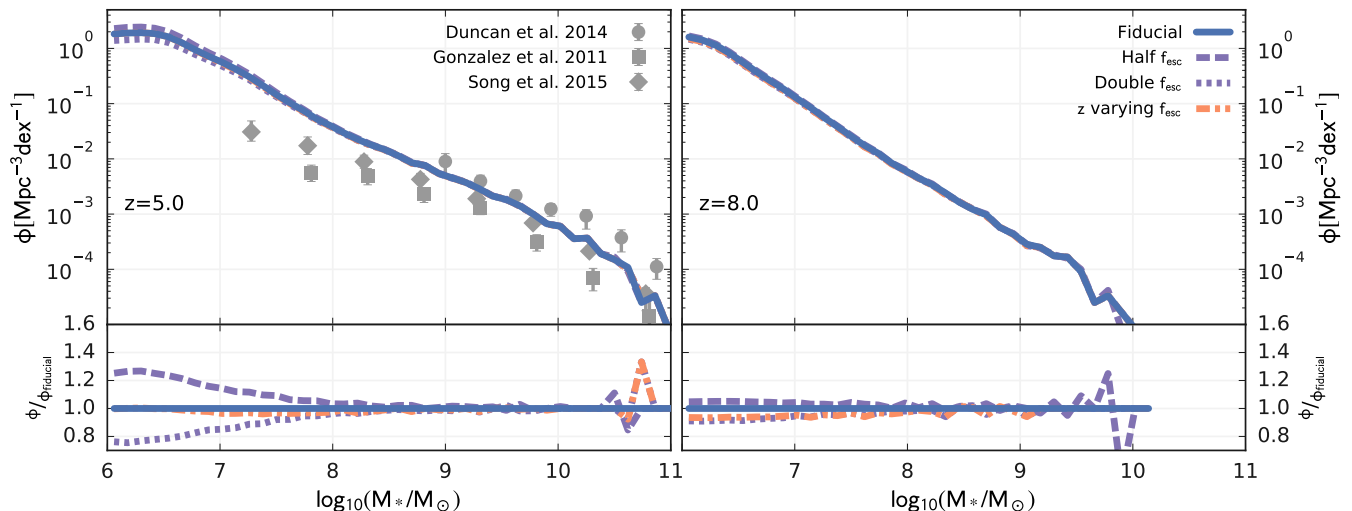


Figure 13. The galaxy stellar mass functions produced by the z -varying f_{esc} model (orange dash-dotted) at $z=7$ and 8. Also shown for comparison are the results of the *fiducial* (solid blue), *half f_{esc}* (purple dashed) and *double f_{esc}* (purple dotted) models. Grey points in the left-hand panel show the observational data used to constrain the *fiducial* model. The early onset of reionization in the z -varying f_{esc} model is largely compensated for by its extended duration, leading to an evolution in the stellar mass function which shows good agreement with our *fiducial* result.

mass is then used in all 21cmFAST calculations. All other semi-analytic model parameters remain fixed to their *fiducial* values. In the bottom panel of Fig. 11 we plot the resulting evolution of the integrated free electron scattering optical depth for this model, demonstrating that it is consistent with the *Planck* constraints.

At $z \gtrsim 17$ the z -varying f_{esc} model escape fraction is large, and the slope of the ionizing emissivity is similar to that of the *fiducial* model. At lower redshifts, f_{esc} begins to decline, leading to a flattening of the \dot{N}_{ion} evolution at $z \lesssim 9$. The presence of this flattening indicates that the escape fraction is declining at a rate which is approximately equal to the growth of stellar mass in the simulation. The resulting slow-down in the rate of ionizing photon emission prolongs the latter stages of reionization, causing the slower evolution of τ_e seen in the bottom panel of Fig. 11.

In Fig. 12, we present the evolution of the volume-weighted global neutral fraction of the z -varying f_{esc} model (orange dash-dotted). The large escape fraction in this model at high- z leads to an early onset of reionization. However, since f_{esc} decreases over time, the speed at which reionization progresses declines with decreasing neutral fraction, resulting in an extended EoR. In Fig. 13, we also present the galaxy stellar mass functions of the z -varying f_{esc} model at $z=5$ and 8. From this, we see that the early onset of reionization is largely compensated for by its extended duration, leading to an evolution in the stellar mass function which shows good agreement with our *fiducial* result.

In summary, we have demonstrated that, for a realistic population of galaxies which match current observational measurements of the growth of stellar mass and electron scattering optical depth, the additional constraining power of the observed post-reionization ionizing emissivity provides potential evidence for the requirement of a varying escape fraction of ionizing photons. This agrees well with the findings of other works using both τ_e and \dot{N}_{ion} as constraints (e.g. Kuhlen & Faucher-Giguère 2012).

4.5 The importance of environment

As demonstrated in Figs 6 and 9, there is excellent agreement between the stellar mass functions and neutral fraction evolutions predicted by the *fiducial* (solid blue) and *homogeneous* (green dashed) reionization prescriptions. Despite this, we show in this section that there can be significant differences in the stellar mass predictions for individual galaxies. We also explore these differences in detail in order to elucidate the important role of environment in modulating the UVB suppression of galaxy growth.

In the top panel of Fig. 14, we show the distribution of fractional changes in individual galaxy stellar masses between the *fiducial* and *homogeneous* models. Contours indicate the 68, 95 and 99% confidence intervals of the distribution, whilst the histograms on the right-hand side show the distribution⁸ of all stellar mass ratios for galaxies in the *fiducial* model with stellar masses larger than $10^{6.7} M_{\odot}$. As expected from the close agreement between the stellar mass functions of these two prescriptions, the distribution is peaked around $M_{*}^{\text{homog}}/M_{*}^{\text{fiducial}}=1$. However, some galaxies exhibit significant variations, especially at lower stellar masses. Below $10^7 M_{\odot}$, it is common for galaxies to vary in mass by factors of 2 or more, with order-of-magnitude differences possible for lower masses. The distribution in galaxy mass ratios at a fixed stellar mass is largely symmetric, meaning that the total stellar functions produced by these two prescriptions remain in good agreement. However, the different predictions for individual galaxy masses may have important consequences for galaxy clustering statistics and 21cm power spectra owing to the Poisson noise that this scatter adds between the halo and galaxy clustering. This highlights that despite the good agreement in stellar

⁸ The plotted curves are a log normalized kernel-density estimate of full marginalized distribution.

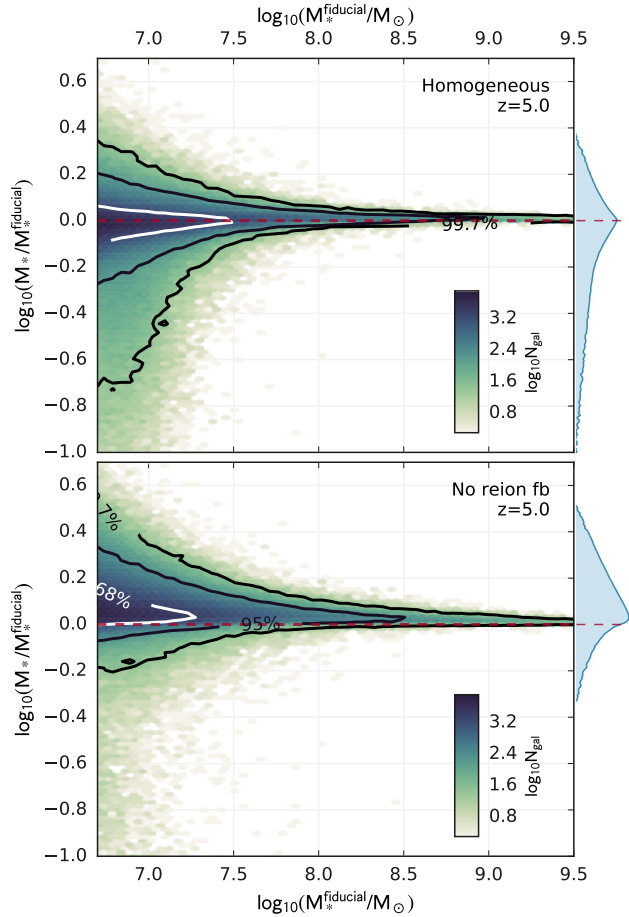


Figure 14. The fractional change in stellar masses of individual galaxies with respect to the *fiducial* model at $z=5$. Contours indicate the 1σ , 2σ and 3σ confidence intervals of each distribution. Blue distributions on the right axes show a log normalized kernel density estimation of the marginalized distribution of stellar mass fractions. The spread in the galaxy masses predicted by the *homogeneous* model compared to the self-consistent, patchy *fiducial* model (top panel) is largely a result of environmental effects which are not fully encoded by the former model. Furthermore, there are a number of galaxies with stellar masses in the *no reionization feedback* model which are less than their counterparts in the *fiducial* feedback case (bottom panel). This highlights the potentially complicated nature of photoionization suppression on the growth of stellar mass in the early Universe.

mass functions, there can be important consequences of using a self-consistent, spatially dependent model of reionization that is not fully encoded in a parametrized homogeneous description.

In the bottom panel of Fig. 14 we plot the same distribution of variations in individual galaxy masses between the *fiducial* and *no reionization feedback* runs. As expected, the bulk of galaxies experience a boost in their masses in the absence of reionization feedback. This is because each galaxy attains access to the full Universal fraction of baryons, even after their surroundings have been fully ionized. There are, however, a small number of galaxies for which the absence of photoionization results in a decreased stellar mass. In the majority of cases, this can be explained by an increase in the

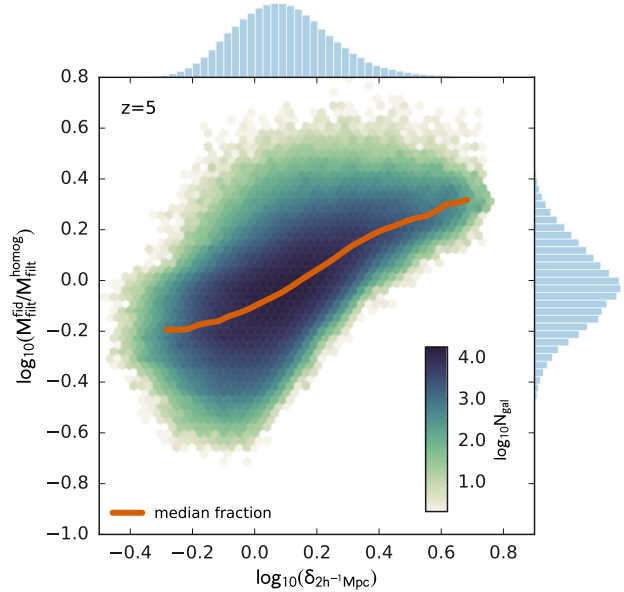


Figure 15. The fractional difference in filtering mass (M_{filt}) values of individual haloes at $z=5$ predicted by the *fiducial* patchy reionization model and the homogeneous parametrized model as a function of total matter density smoothed over a $2h^{-1}$ Mpc scale. Histograms on the right and top axes indicate the marginalized distributions of filtering mass ratios and densities, respectively. There is a clear trend of increasing M_{filt} (i.e. more effective photoionization suppression) with increasing environmental density in the *fiducial* model which is not captured in the simple homogeneous case. This can be easily understood as the effect of UVB suppression from ionizing photons produced by nearby galaxies in over-dense environments, an effect which is not fully included in the parametrized *homogeneous* model.

number of galaxies populating low-mass haloes. In the *fiducial* model, infall into these low-mass haloes is suppressed due to the ionizing background. Thus, when they are accreted into larger systems, with deeper potential wells, their new parents are able to accrete the previously photoheated to fuel new star formation. However, in the *no reionization feedback* model, the absence of the ionizing background allows many small haloes to accrete baryons which then cool and condense down into a galaxy. When these haloes are eventually accreted into larger systems, their baryons remain locked up in the infalling satellite, making them unavailable to fuel the growth of the central galaxy. In addition, small satellite galaxies often have extremely long merger times (cf. Equation 25), further compounding their ability to keep baryons locked up in the form of stars and cold gas. The net effect is that the stellar mass of their host halo's central galaxy can actually go down in the absence of reionization feedback, again highlighting the potentially complicated effects of photoionization suppression on the growth of stellar mass in the early Universe.

In Fig. 15, we plot a 2D histogram of the ratio of filtering mass values (M_{filt} ; cf. Equation 32) predicted by the *fiducial* and *homogeneous* models for each FoF group at $z=5$, as a function of the local total matter density smoothed on a $2h^{-1}$ Mpc scale. The histogram on the right-hand axes indicates the distribution of filtering mass ratios marginalized

over all environmental densities. We find that the patchy *fiducial* model predicts a photoionization suppression which depends on environment with up to an order of magnitude difference in the filtering mass between over- and underdense regions. The trend of increasing filtering mass with increasing over-density can be seen more clearly by considering the median filtering mass ratio as a function of environment (solid orange line) and is due to the contribution of ionizing flux from nearby galaxies which is not self-consistently included in the *homogeneous* model. At higher local densities, there is an increase in the average number and mass of nearby sources contributing ionizing photons which in the *fiducial*, patchy reionization model results in an increased M_{filt} value.

The inability of parametrized global reionization prescriptions to capture the density-dependent spread in filtering masses, as well as the trend of increasing filtering mass with density, could have important consequences for the galaxy clustering and cross-correlation statistics. It is also important to note that we were only able to calibrate the homogeneous variation through the use of our full fiducial run with self-consistently coupled reionization. Any change to the free model parameters listed in Table 1, or underlying cosmological model, would require the mean $M_{\text{filt}}-z$ relationship to be recalculated.

5 CONCLUSIONS

In this work we have presented a new semi-analytic galaxy formation model, MERAXES, developed as part of the DRAGONS programme. MERAXES has been designed to investigate the growth of the first galaxies and their role in driving the EoR. It possesses the following key features.

- A temporally and spatially coupled treatment of reionization provided by the integration of the semi-numerical reionization model 21CMFAST (Section 2.11).
- The use of accurate hierarchical merger trees extracted from a custom N -body simulation with a large volume and high mass resolution, as well as the temporal resolution required to resolve star formation and supernova feedback in the early Universe (Section 2.1).
- Galaxy formation physics based on the Croton et al. (2006) semi-analytic model, with updates to deal with the high temporal resolution provided by our input merger trees such as a time-delayed supernova feedback prescription and the removal of the instantaneous recycling approximation (Sections 2.2–2.10).

We have calibrated the free parameters of MERAXES against the observed evolution of the galaxy stellar mass function between $5 \leq z \leq 7$, the latest *Planck* (Planck Collaboration 2015) constraints on the electron optical scattering depth (Section 3), and the Lyman α forest constraints on the $z \lesssim 6$ ionizing emissivity (Section 4.4.1). Through the subsequent investigation of a number of model runs with varying reionization and galaxy feedback parameters, we find the following key results.

- Supernova feedback is the dominant physical mechanism for regulating the growth of galaxy stellar mass both during and immediately prior to reionization. We find that

it is only in the absence of supernova feedback that suppression of star formation due to the presence of an ionizing UVB reaches significant levels, and even then, only if star formation is efficient enough so as to be gas supply limited.

- We further find that the reionization history of the IGM is similarly insensitive to reionization feedback. This implies that the process of reionization is not self-regulated (Section 4.3)⁹.

- The *fiducial* model also predicts that a broad range of halo masses contribute to ionizing photon production during reionization (Section 4.3).

- Models employing a constant escape fraction of ionizing photons are unable to simultaneously match the observed growth of galaxy stellar mass, Thomson scattering optical depth measurements, and the Lyman α forest constraints on the $z \lesssim 6$ global ionizing emissivity. However, we show that an evolving escape fraction, with $0.05 \lesssim f_{\text{esc}} \lesssim 0.1$ at $z \sim 6$ and a redshift scaling proportional to $(1+z)^\kappa$, where $\kappa \sim 3$, does allow our model to simultaneously satisfy these constraints. (Section 4.4).

- Using our framework we are able to quantify the effect of reionization on the shape and normalization of the stellar mass function, finding no observationally detectable imprint for stellar masses of $M_* > 10^{7.5}$ at $z \geq 5$ (Section 4.2).

- By comparing to a simple, homogeneous reionization prescription of the kind traditionally used in semi-analytic models, we find that the inclusion of a self-consistent patchy reionization model can result in significant, environmentally dependent variations in the stellar masses of individual galaxies by factors of 2–3 (Section 4.5).

The scatter and density-dependent effects of UVB suppression could have important consequences for galaxy clustering and cross-correlation statistics. These could in turn lead to detectable signatures in the 21 cm power spectrum measurements of current and upcoming radio surveys. The ability to self-consistently include and quantify these effects is a key feature of MERAXES and the DRAGONS programme and is investigated in detail in Paper V.

In this work, we have chosen to calibrate our model against the high- z stellar mass function. However, a more directly observable quantity is UV luminosity. In Paper IV, we demonstrate the excellent agreement of our fiducial model with the observed UV luminosity function over a broad range in redshift ($5 < z < 10$), allowing us to further investigate the validity of the commonly used Kennicutt relation (Kennicutt 1998; Madau et al. 1998) to approximate galaxy star formation rates from UV luminosities at high- z .

Finally, we note that we have chosen to base the galaxy physics of our initial MERAXES implementation on the Croton et al. (2006) model in order to provide confidence in our newly developed framework and to allow us to test the relative effects of supernova and reionization feedback for a set of well-understood and tested physics prescriptions. However, in future work we will expand upon MERAXES, adapting and improving the model to provide a better match with the results of our suite of hydrodynamical simulations,

⁹ However, we note that if the process of reionization is more extended than is predicted by our model (for example, due to inhomogeneous recombinations in the IGM) then reionization feedback may play a more effective role.

Smaug (Duffy et al. 2014), run as part of the DRAGONS programme.

ACKNOWLEDGEMENTS

This research was supported by the Victorian Life Sciences Computation Initiative (VLSCI), grant ref. UOM0005, on its Peak Computing Facility hosted at the University of Melbourne, an initiative of the Victorian Government, Australia. Part of this work was performed on the gSTAR national facility at Swinburne University of Technology. gSTAR is funded by Swinburne and the Australian Governments Education Investment Fund. AM acknowledges support from the European Research Council (ERC) under the European Unions Horizon 2020 research and innovation programme (grant agreement no. 638809 AIDA). This research programme is funded by the Australian Research Council through the ARC Laureate Fellowship FL110100072 awarded to JSBW.

REFERENCES

- Angel P. W., Poole G. B., Ludlow A. D., Duffy A. R., Geil P. M., Mutch S. J., Mesinger A., Wyithe J. S. B., 2016, *MNRAS*, 459, 2106
- Barkana R., Loeb A., 2001, *Phys. Rep.*, 349, 125
- Baugh C. M., 2006, *Rep. Prog. Phys.*, 69, 3101
- Becker G. D., Bolton J. S., 2013, *MNRAS*, 436, 1023
- Behroozi P. S., Wechsler R. H., Conroy C., 2013a, *ApJ*, 762, L31
- Behroozi P. S., Wechsler R. H., Conroy C., 2013b, *ApJ*, 770, 57
- Benson A. J., Lacey C. G., Baugh C. M., Cole S., Frenk C. S., 2002, *MNRAS*, 333, 156
- Benson A. J., Sugiyama N., Nusser A., Lacey C. G., 2006, *MNRAS*, 369, 1055
- Binney J., Tremaine S., 2008, *Galactic Dynamics: Second Edition*. Princeton University Press, Princeton, NJ
- Bolton J. S., Haehnelt M. G., 2007, *MNRAS*, 382, 325
- Bournaud F. et al., 2014, *ApJ*, 780, 57
- Bouwens R. J. et al., 2011, *ApJ*, 737, 90
- Bower R. G., Benson A. J., Malbon R., Helly J. C., Frenk C. S., Baugh C. M., Cole S., Lacey C. G., 2006, *MNRAS*, 370, 645
- Boylan-Kolchin M., Ma C.-P., Quataert E., 2008, *MNRAS*, 383, 93
- Bullock J. S., Dekel A., Kolatt T. S., Kravtsov A., Klypin A., Porciani C., Primack J. R., 2001, *ApJ*, 555, 240
- Chen P., Wise J. H., Norman M. L., Xu H., O’Shea B. W., 2014, *ApJ*, 795, 144
- Ciardi B., Stoehr F., White S. D. M., 2003, *MNRAS*, 343, 1101
- Cole S., Lacey C. G., Baugh C. M., Frenk C. S., 2000, *MNRAS*, 319, 168
- Cox T. J., Primack J., Jonsson P., Somerville R. S., 2004, *ApJ*, 607, L87
- Croton D. J. et al., 2006, *MNRAS*, 365, 11
- De Lucia G., Blaizot J., 2007, *MNRAS*, 375, 2
- De Lucia G., Kauffmann G., White S. D. M., 2004, *MNRAS*, 349, 1101
- Díaz C. G., Koyama Y., Ryan-Weber E. V., Cooke J., Ouchi M., Shimasaku K., Nakata F., 2014, *MNRAS*, 442, 946
- Dijkstra M., Haiman Z., Rees M. J., Weinberg D. H., 2004, *ApJ*, 601, 666
- Duffy A. R., Wyithe J. S. B., Mutch S. J., Poole G. B., 2014, *MNRAS*, 443, 3435
- Duncan K. et al., 2014, *MNRAS*, 444, 2960
- Eddington A. S., 1913, *MNRAS*, 73, 359
- Feng Y., Di-Matteo T., Croft R. A., Bird S., Battaglia N., Wilkins S., 2016, *MNRAS*, 455, 2778
- Finlator K., Davé R., Özel F., 2011, *ApJ*, 743, 169
- Furlanetto S. R., 2006, *New Astron. Rev.*, 50, 157
- Furlanetto S. R., Zaldarriaga M., Hernquist L., 2004, *ApJ*, 613, 1
- Geil P. M., Mutch S. J., Poole G. B., Angel P. W., Duffy A. R., Mesinger A., Wyithe J. S. B., 2015, preprint (arXiv: e-prints) (Paper V)
- Geil P. M., Wyithe J. S. B., 2008, *MNRAS*, 386, 1683
- Genel S. et al., 2014, *MNRAS*, 445, 175
- Glazebrook K., 2013, *Publ. Astron. Soc. Australia*, 30, 56
- Gnedin N. Y., 2000, *ApJ*, 542, 535
- Gnedin N. Y., Kravtsov A. V., Chen H.-W., 2008, *ApJ*, 672, 765
- González V., Labbe I., Bouwens R. J., Illingworth G., Franx M., Kriek M., 2011, *ApJ Letters*, 735, L34
- Grazian A. et al., 2015, *A&A*, 575, A96
- Grogin N. A. et al., 2011, *ApJS*, 197, 35
- Guo Q., White S., Angulo R. E., Henriques B., Lemson G., Boylan-Kolchin M., Thomas P., Short C., 2013, *MNRAS*, 428, 1351
- Guo Q. et al., 2011, *MNRAS*, 413, 101
- Harker G., Cole S., Helly J., Frenk C., Jenkins A., 2006, *MNRAS*, 367, 1039
- Henriques B. M. B., White S. D. M., Thomas P. A., Angulo R., Guo Q., Lemson G., Springel V., Overzier R., 2015, *MNRAS*, 451, 2663
- Henriques B. M. B., White S. D. M., Thomas P. A., Angulo R. E., Guo Q., Lemson G., Springel V., 2013, *MNRAS*, 431, 3373
- Hopkins P. F. et al., 2010, *ApJ*, 724, 915
- Iliev I. T., Mellema G., Pen U.-L., Bond J. R., Shapiro P. R., 2008, *MNRAS*, 384, 863
- Iliev I. T., Pen U.-L., Bond J. R., Mellema G., Shapiro P. R., 2007, *ApJ*, 660, 933
- Jaacks J., Nagamine K., Choi J. H., 2012, *MNRAS*, 427, 403
- Jeon M., Pawlik A. H., Bromm V., Milosavljević M., 2014, *MNRAS*, 444, 3288
- Kauffmann G., 1996, *MNRAS*, 281, 475
- Kennicutt R. C., 1989, *ApJ*, 344, 685
- Kennicutt R. C. J., 1998, *ApJ*, 498, 541
- Kim H.-S., Wyithe J. S. B., Park J., Lacey C. G., 2013a, *MNRAS*, 433, 2476
- Kim H.-S., Wyithe J. S. B., Raskutti S., Lacey C. G., Helly J. C., 2013b, *MNRAS*, 428, 2467
- Koekemoer A. M. et al., 2011, *ApJS*, 197, 36
- Kravtsov A. V., Gnedin O. Y., Klypin A. A., 2004, *ApJ*, 609, 482
- Kuhlen M., Faucher-Giguère C.-A., 2012, *MNRAS*, 423, 862
- Lacey C. G., Baugh C. M., Frenk C. S., Benson A. J., 2011, *MNRAS*, 412, 1828
- Lagos C. d. P., Bayet E., Baugh C. M., Lacey C. G., Bell T. A., Fanidakis N., Geach J. E., 2012, *MNRAS*, 426, 2142
- Leroy A. K., Walter F., Brinks E., Bigiel F., de Blok W. J. G., Madore B., Thornley M. D., 2008, *AJ*, 136, 2782
- Liu C., Mutch S. J., Angel P. W., Duffy A. R., Geil P. M., Poole G. B., Mesinger A., Wyithe J. S. B., 2015, preprint (arXiv: e-prints) (Paper IV)
- Lu Y., Kereš D., Katz N., Mo H. J., Fardal M., Weinberg M. D., 2011a, *MNRAS*, 416, 660
- Lu Y., Mo H. J., Weinberg M. D., Katz N., 2011b, *MNRAS*, 416, 1949
- Madau P., Pozzetti L., Dickinson M., 1998, *ApJ*, 498, 106
- Martin C. L., 1999, *ApJ*, 513, 156
- McLure R. J. et al., 2013, *MNRAS*, 432, 2696
- McQuinn M., Oh S. P., Faucher-Giguère C.-A., 2011, *ApJ*, 743, 82
- Mesinger A., Dijkstra M., 2008, *MNRAS*, 390, 1071
- Mesinger A., Furlanetto S., 2007, *ApJ*, 669, 663
- Mesinger A., Furlanetto S., Cen R., 2011, *MNRAS*, 411, 955
- Mitra S., Ferrara A., Choudhury T. R., 2013, *MNRAS*, 428, L1

- Morales M. F., Wyithe J. S. B., 2010, *ARA&A*, 48, 127
- Murray N., Quataert E., Thompson T. A., 2005, *ApJ*, 618, 569
- Mutch S. J., Poole G. B., Croton D. J., 2013, *MNRAS*, 428, 2001
- Norman M. L., Reynolds D. R., So G. C., Harkness R. P., Wise J. H., 2015, *ApJS*, 216, 16
- Ocvirk P. et al., 2015, preprint (arXiv: e-prints)
- Paardekooper J.-P., Khochfar S., Dalla Vecchia C., 2015, *MNRAS*, 451, 2544
- Paardekooper J.-P., Pelupessy F. I., Altay G., Kruip C. J. H., 2011, *A&A*, 530, A87
- Pawlik A. H., Schaye J., Dalla Vecchia C., 2015, *MNRAS*, 451, 1586
- Peng Y., Maiolino R., Cochrane R., 2015, *Nat*, 521, 192
- Planck Collaboration, 2015, preprint (arXiv: e-prints)
- Poole G. B., Angel P. W., Mutch S. J., Power C., Duffy A. R., Geil P. M., Mesinger A., Wyithe S. B., 2016, *MNRAS*, 459, 3025 (Paper I)
- Portinari L., Chiosi C., Bressan A., 1998, *A&A*, 334, 505
- Raičević M., Theuns T., Lacey C., 2011, *MNRAS*, 410, 775
- Robertson B. E. et al., 2013, *ApJ*, 768, 71
- Salpeter E. E., 1955, *ApJ*, 121, 161
- Salvaterra R., Ferrara A., Dayal P., 2011, *MNRAS*, 414, 847
- Schaye J. et al., 2015, *MNRAS*, 446, 521
- Schenker M. A. et al., 2013, *ApJ*, 768, 196
- Shin M.-S., Trac H., Cen R., 2008, *ApJ*, 681, 756
- So G. C., Norman M. L., Reynolds D. R., Wise J. H., 2014, *ApJ*, 789, 149
- Sobacchi E., Mesinger A., 2013, *MNRAS*, 432, 3340
- Sobacchi E., Mesinger A., 2013, *MNRAS*, 432, 51
- Sobacchi E., Mesinger A., 2014, *MNRAS*, 440, 1662
- Sokasian A., Abel T., Hernquist L., 2003, *MNRAS*, 340, 473
- Somerville R. S., Hopkins P. F., Cox T. J., Robertson B. E., Hernquist L., 2008, *MNRAS*, 391, 481
- Somerville R. S., Primack J. R., Faber S. M., 2001, *MNRAS*, 320, 504
- Song M. et al., 2016, *ApJ*, 825, 5
- Springel V. et al., 2005, *Nat*, 435, 629
- Springel V., White S. D. M., Tormen G., Kauffmann G., 2001, *MNRAS*, 328, 726
- Sutherland R. S., Dopita M. A., 1993, *ApJS*, 88, 253
- Thoul A. A., Weinberg D. H., 1996, *ApJ*, 465, 608
- Trac H., Cen R., 2007, *ApJ*, 671, 1
- Trac H., Cen R., Loeb A., 2008, *ApJ*, 689, L81
- Trenti M., Perna R., Jimenez R., 2015, *ApJ*, 802, 103
- Uhlig M., Pfrommer C., Sharma M., Nath B. B., Enßlin T. A., Springel V., 2012, *MNRAS*, 423, 2374
- van den Bosch F. C., Aquino D., Yang X., Mo H. J., Pasquali A., McIntosh D. H., Weinmann S. M., Kang X., 2008, *MNRAS*, 387, 79
- White S. D. M., Frenk C. S., 1991, *ApJ*, 379, 52
- Wise J. H., Cen R., 2009, *ApJ*, 693, 984
- Wisnioski E. et al., 2011, *MNRAS*, 417, 2601
- Wyithe J. S. B., Loeb A., 2003, *ApJ*, 586, 693
- Wyithe J. S. B., Loeb A., 2004, *Nat*, 432, 194
- Wyithe J. S. B., Loeb A., 2013, *MNRAS*, 428, 2741
- Yajima H., Choi J.-H., Nagamine K., 2011, *MNRAS*, 412, 411
- Zahn O., Lidz A., McQuinn M., Dutta S., Hernquist L., Zaldarriaga M., Furlanetto S. R., 2007, *ApJ*, 654, 12
- Zhou J., Guo Q., Liu G.-C., Yue B., Xu Y.-D., Chen X.-L., 2013, *Re. Astron. Astrophys.*, 13, 373

Table A1. The particle masses and box sizes of each of the N -body simulations from the *Tiamat* suite used here.

Simulation	Particle mass (M_{\odot})	Box side length (Mpc)
<i>Tiamat</i>	3.9×10^6	100
<i>Medi Tiamat</i>	1.2×10^6	33.3
<i>Tiny Tiamat</i>	1.0×10^5	14.8

APPENDIX A: MASS RESOLUTION

Throughout this work we run MERAXES on the output of the *Tiamat* collisionless N -body simulation. Here we make use of two complimentary simulations in the DRAGONS suite to quantify the halo and stellar masses down to which *Tiamat* is complete, as well as the total fraction of stellar mass (and hence ionizing photons) which may be missed due to halo mass resolution. The names, particle masses and box sizes of each simulation are presented in Table A1.

A1 Halo mass

In the left panel of Fig. A1 we show the FoF group mass functions for all three simulations at $z=6, 8, 10$ and 12 . The turn overs at low masses are a direct result of limited mass resolution. Vertical lines indicate the atomic cooling mass thresholds (M_{cool}) at each of these redshifts. In MERAXES, galaxy formation only occurs in haloes above M_{cool} . Therefore a fully resolved simulation would ideally identify all haloes above this value at all redshifts $\lesssim 15$. *Tiny Tiamat* with its low particle mass is easily able to achieve this.

The top-right panel of Fig. A1 shows a zoom-in of the mass functions near to M_{cool} , whilst the bottom-right panel shows the fractional difference in number density with respect to the *Tiny Tiamat* results. From this we can see that *Medi Tiamat* is complete to within 10% down to $M_{\text{vir}}=M_{\text{cool}}$ at $z=6$. *Tiamat* is complete to within the same fractional difference down to $M_{\text{vir}}=10^{8.8} M_{\odot}$, which is approximately 0.5dex above the atomic cooling mass threshold at this redshift. Since the mass resolution of all simulations remains fixed whilst the value of the atomic cooling mass threshold decreases with increasing redshift, both *Tiamat* and *Medi Tiamat* effectively miss a larger fraction of haloes at earlier times.

A2 Stellar mass

In Section 4.1 we demonstrate that supernova feedback curtails star formation in low mass haloes. As a result, although *Tiamat* is not complete in halo number density all the way down to the atomic cooling mass threshold, the fraction of stellar mass (and therefore ionizing photons) which is unresolved is far less. In the left hand panel of Fig. A2 we show the galaxy stellar mass functions calculated using the *no reionization feedback* model run on each N -body simulation. The free parameters of MERAXES remain fixed between simulations so that any differences between the results of each are a direct consequence of mass resolution and volume.

Compared to the FoF group halo mass functions (Fig. A1), the difference in the position of the resolution

limit turnovers between simulations is greatly reduced. The upper-right panel of Fig. A2 shows a zoom-in of the mass functions around the turn over positions. The lower-right panel again shows the fractional difference in number density with respect to *Tiny Tiamat* which resolves all haloes down to M_{cool} and beyond (see Section A1 above). Here we can see that *Medi Tiamat* reaches the turnover in galaxy number density predicted by *Tiny Tiamat* to within 0.1dex at all redshifts shown. It does, however, predict a lower normalization in the mass function by around 20% on average across all redshifts shown. This is predominantly a consequence of cosmic variance, driven by the small box size of both simulations (and in particular *Tiny Tiamat*). The turnover in the stellar mass function predictions of *Tiamat* occurs at masses approximately 0.2–0.3dex higher than *Tiny Tiamat* at all redshifts.

In the top panel of Fig. A3 we plot the cumulative stellar mass of each simulation (again predicted by the *no reionization feedback* model) as a function of FoF group virial mass. The bottom panel indicates the fractional difference between the simulations, this time with respect to *Medi Tiamat*. We have chosen to utilize *Medi Tiamat* as our reference here since it achieves a good compromise between mass resolution and volume, as demonstrated above. *Tiny Tiamat*, on the other hand, fails to capture the most massive haloes at any redshift due to its limited volume. This biases the cumulative masses predicted by this simulation downwards. At $z=6$, we find that *Tiamat* recovers 97% of all stellar mass (and therefore ionizing photons) above the atomic cooling mass threshold. The fraction falls to 90% at $z=8$ and 75% at $z=10$.

This paper has been typeset from a $\text{\TeX}/\text{\LaTeX}$ file prepared by the author.

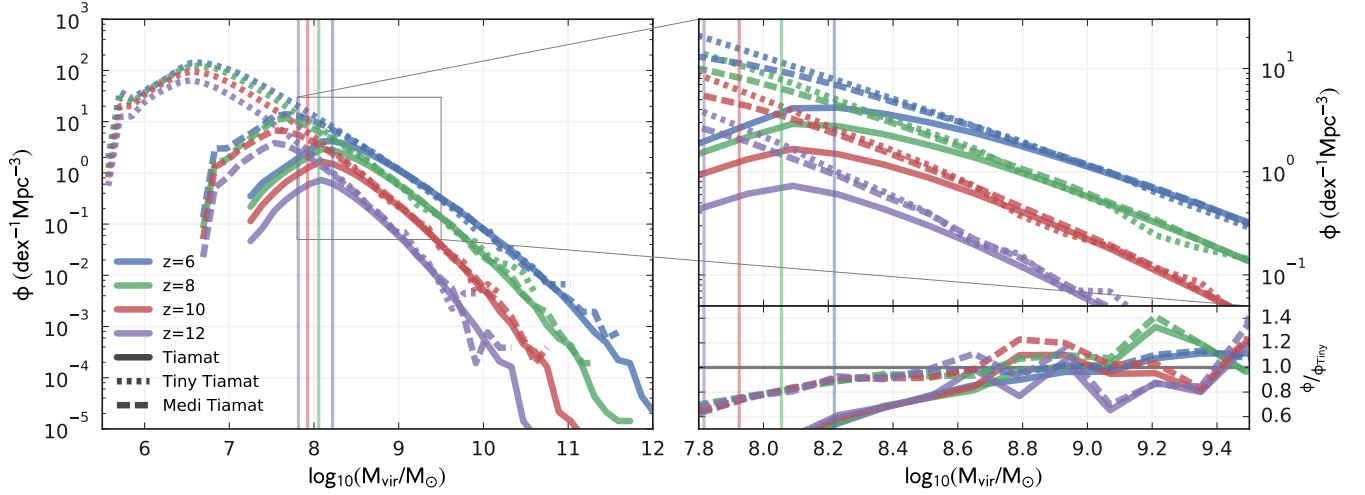


Figure A1. The FoF group halo mass functions of the *Tiny Tiamat* (dotted), *Medi Tiamat* (dashed), and full *Tiamat* (solid) simulations at redshifts 6–12. Vertical lines indicate the atomic cooling mass threshold at each redshift plotted. The right-hand panel shows a zoom in of the mass functions (top), along with the fractional difference in number density of the *Tiamat* and *Medi Tiamat* simulations with respect to the *Tiny Tiamat* results (bottom).

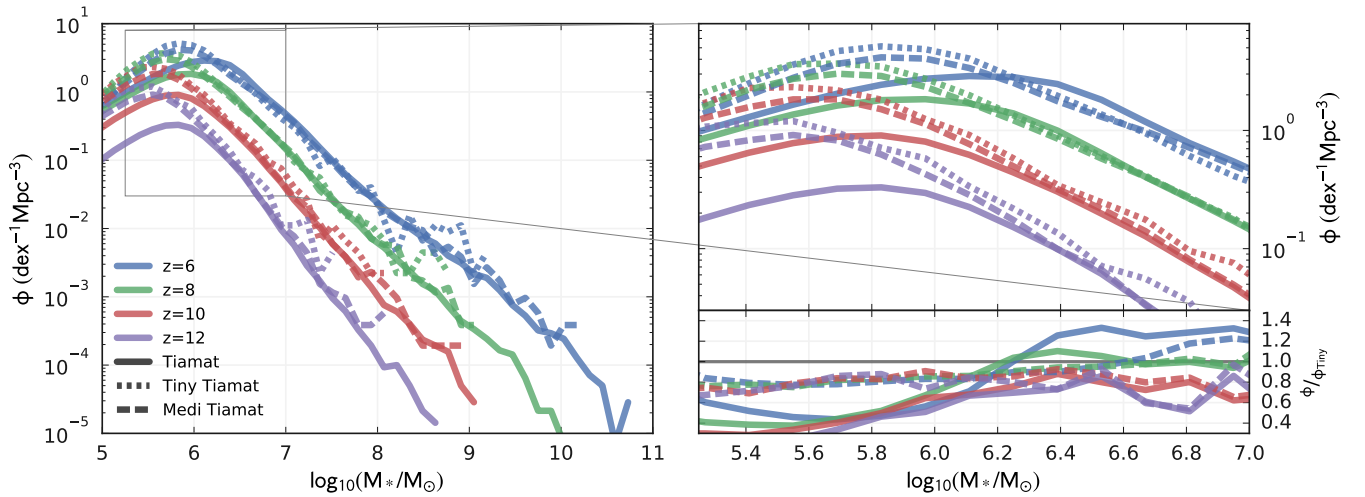


Figure A2. The galaxy stellar mass function produced by the *no reionization feedback* MERAXES model variation run on the merger trees extracted from the *Tiny Tiamat* (dotted), *Medi Tiamat* (dashed), and full *Tiamat* (solid) simulations at redshifts 6–12. The right-hand panel shows a zoom in of the mass functions (top), along with the fractional difference in number density of the *Tiamat* and *Medi Tiamat* simulations with respect to the *Tiny Tiamat* results (bottom).

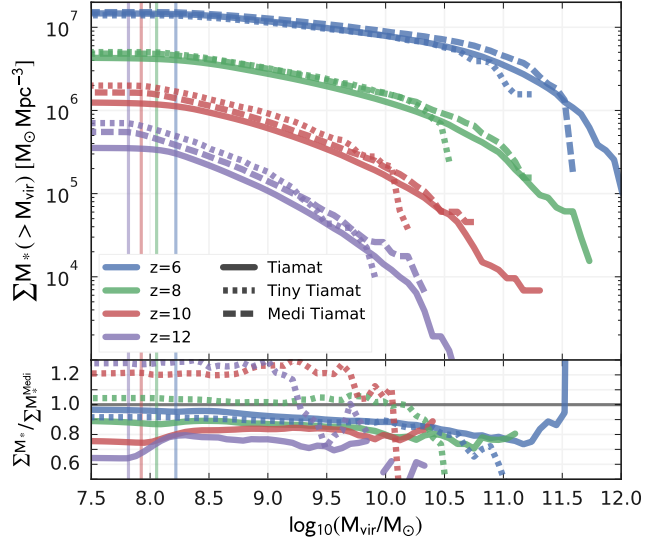


Figure A3. Cumulative stellar mass as a function of FoF group mass predicted by the *no reionization feedback* MERAXES model variation run on the merger trees extracted from the *Tiny Tiamat* (dotted), *Medi Tiamat* (dashed), and full *Tiamat* (solid) simulations at redshifts 6–12. The lower panel shows the fractional difference with respect to the *Medi Tiamat* results.